

See discussions, stats, and author profiles for this publication at: <https://www.researchgate.net/publication/239722011>

# Spectroscopic and Modeling Investigations of the Gas Phase Chemistry and Composition in Microwave Plasma Activated B<sub>2</sub>H<sub>6</sub>/CH<sub>4</sub>/Ar/H<sub>2</sub> Mixtures

ARTICLE in THE JOURNAL OF PHYSICAL CHEMISTRY A · SEPTEMBER 2010

Impact Factor: 2.69 · DOI: 10.1021/jp104532y · Source: PubMed

---

CITATIONS

12

---

READS

22

5 AUTHORS, INCLUDING:



Yuri Mankelevich

Lomonosov Moscow State University

148 PUBLICATIONS 1,552 CITATIONS

SEE PROFILE

# Spectroscopic and Modeling Investigations of the Gas Phase Chemistry and Composition in Microwave Plasma Activated B<sub>2</sub>H<sub>6</sub>/CH<sub>4</sub>/Ar/H<sub>2</sub> Mixtures

Jie Ma,<sup>†</sup> James C. Richley, David R. W. Davies, and Michael N. R. Ashfold\*

School of Chemistry, University of Bristol, Bristol, United Kingdom, BS8 1TS

Yuri A. Mankelevich

Skobel'tsyn Institute of Nuclear Physics, Moscow State University, Leninskie gory, Moscow, 119991 Russia

Received: May 18, 2010; Revised Manuscript Received: July 31, 2010

A comprehensive study of microwave (MW) activated B<sub>2</sub>H<sub>6</sub>/CH<sub>4</sub>/Ar/H<sub>2</sub> plasmas used for the chemical vapor deposition of B-doped diamond is reported. Absolute column densities of ground state B atoms, electronically excited H(*n* = 2) atoms, and BH, CH, and C<sub>2</sub> radicals have been determined by cavity ring down spectroscopy, as functions of height (*z*) above a molybdenum substrate and of the plasma process conditions (B<sub>2</sub>H<sub>6</sub>, CH<sub>4</sub>, and Ar partial pressures; total pressure, *p*; and supplied MW power, *P*). Optical emission spectroscopy has also been used to explore variations in the relative densities of electronically excited H atoms, H<sub>2</sub> molecules, and BH, CH, and C<sub>2</sub> radicals, as functions of the same process conditions. These experimental data are complemented by extensive 2D(*r*, *z*) modeling of the plasma chemistry, which result in substantial refinements to the existing B/C/H/O thermochemistry and chemical kinetics. Comparison with the results of analogous experimental/modeling studies of B<sub>2</sub>H<sub>6</sub>/Ar/H<sub>2</sub> and CH<sub>4</sub>/Ar/H<sub>2</sub> plasmas in the same MW reactor show that: (i) trace B<sub>2</sub>H<sub>6</sub> additions have negligible effect on a pre-established CH<sub>4</sub>/Ar/H<sub>2</sub> plasma; (ii) the spatial extent of the B and BH concentration profiles in a B<sub>2</sub>H<sub>6</sub>/CH<sub>4</sub>/Ar/H<sub>2</sub> plasma is smaller than in a hydrocarbon-free B<sub>2</sub>H<sub>6</sub>/Ar/H<sub>2</sub> plasma operating at the same *p*, *P*, etc.; (iii) B/C coupling reactions (probably supplemented by reactions involving trace O<sub>2</sub> present as air impurity in the process gas mixture) play an important role in determining the local BH<sub>*x*</sub> (*x* = 0–3) radical densities; and (iv) gas phase B atoms are the most likely source of the boron that incorporates into the growing B-doped diamond film.

## 1. Introduction

Semiconducting diamond has long been recognized as a hugely promising material for application in high power and high temperature electronic devices.<sup>1–3</sup> Reliable growth of high quality n-type diamond remains a challenge, but p-type diamond with good conductivity is now achieved quite routinely by incorporating boron into the diamond lattice during growth by chemical vapor deposition (CVD).<sup>1–5</sup> Electronic devices based on B-doped diamond that are attracting particular interest at present include the boron δ doped p-channel field effect transistor (FET)<sup>6–8</sup> and a Schottky diode.<sup>9–11</sup> The δ doping application requires growth of an ultrathin (a few nanometers) B-doped layer within a sandwich structure, with interfaces that are sharply defined to a similar resolution. The diode requires growth of layers that are, respectively, heavily and weakly B-doped. For both applications, control and reproducibility of the growth and doping processes are critical. B-doped diamond has also been shown to be superconductive at low temperatures,<sup>12–14</sup> and given its chemical inertness, good conductivity, biocompatibility, and high electrochemical potential, it is seen as a very promising material for biosensing applications.<sup>15,16</sup> Despite this growing range of applicability, however, our understanding of the gas-phase and gas-surface chemistry that underpins B-doped diamond CVD is very far from complete.

The most commonly used boron source gas in B-doped diamond CVD is B<sub>2</sub>H<sub>6</sub> which, for safety reasons, is used heavily diluted in H<sub>2</sub> (200 ppm B<sub>2</sub>H<sub>6</sub> in most of the present experiments). During diamond deposition, a small amount of B<sub>2</sub>H<sub>6</sub>/H<sub>2</sub> mixture is added to the CH<sub>4</sub>/Ar/H<sub>2</sub> plasma and converted into various “active” BH<sub>*x*</sub> (*x* = 0–3) species, some of which (at least) are then able to accommodate into the growing diamond film through a complex sequence of gas–surface encounters and surface rearrangement reactions.<sup>17</sup>

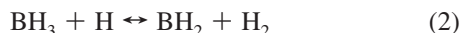
The literature contains many reports of studies that have attempted to establish correlations between the properties of the as-grown diamond (e.g., film quality, growth rates, dopant concentrations, etc.) and plasma and other operational parameters like B<sub>2</sub>H<sub>6</sub> flow rate, [B]/[C] ratio in the source gas mixture, or substrate temperature (*T*<sub>sub</sub>).<sup>18–20</sup> but few in situ diagnostic studies of B-containing activated gas mixtures have yet been reported.<sup>21–25</sup> The first optical emission spectroscopy (OES) diagnostic studies of a microwave (MW) activated B<sub>2</sub>H<sub>6</sub>/Ar/H<sub>2</sub> plasma<sup>21</sup> used a high resolution spectrometer to resolve BH\* and H<sub>2</sub>\* emission features and thereby estimate the rotational temperature (*T*<sub>rot</sub>) and thus the gas temperature, *T*<sub>gas</sub>. Spectral overlap within the P branch of the BH(A<sup>1</sup>Π→X<sup>1</sup>Σ<sup>+</sup>) (0,0) band dictated that only a limited number of R branch transitions could be used in the *T*<sub>rot</sub> determinations, but the values so derived agreed well with temperature values estimated from analysis of the rotational structure in the H<sub>2</sub>\* emissions. The same group later reported a combined OES (in the UV/visible region) and infrared (IR) tunable diode laser absorption spectroscopy investigation of B<sub>2</sub>H<sub>6</sub>/Ar/H<sub>2</sub> plasmas.<sup>22</sup> The latter technique

\* To whom correspondence should be addressed. Phone: (117)-9288312/3. Fax: (117)-9250612. E-mail: mike.ashfold@bris.ac.uk.

<sup>†</sup> Present address: Clark Hall 160, Department of Physics, Cornell University, Ithaca, NY 14853, U.S.A.

allowed monitoring of B<sub>2</sub>H<sub>6</sub>, BH<sub>3</sub>, and BH absorptions as a function of input MW power, while the former provided estimates of  $T_{\text{gas}}$ , the electron temperature ( $T_e$ ) and suggested a possible OES-based means of determining absolute B densities in such plasmas.

Within the context of B-doped diamond CVD, it is important to note that the above measurements were all performed in carbon-free plasmas, and at much lower pressures and higher B<sub>2</sub>H<sub>6</sub> mole fractions than are used in B-doped diamond growth. Gicquel and co-workers, in contrast, have investigated MW activated B<sub>2</sub>H<sub>6</sub>/CH<sub>4</sub>/Ar/H<sub>2</sub> plasmas under conditions that are immediately relevant to B-doped diamond growth. They have highlighted the inevitable overlap between the BH(A → X) (0,0) R branch and the (generally much more intense) CH(A<sup>2</sup>Δ → X<sup>2</sup>Π) emission, which precludes use of the former as a way of estimating  $T_{\text{gas}}$  in B<sub>2</sub>H<sub>6</sub>/CH<sub>4</sub>/Ar/H<sub>2</sub> plasmas.<sup>23</sup> Fortunately, however, the BH(A → X) (0,0) Q branch is not overlapped by CH\* emissions. The Q branch lines are too closely spaced to be resolved in an OES experiment, but Rayar et al.<sup>23</sup> have shown that the band envelope is a sensitive function of  $T_{\text{rot}}$  and, given the appropriate spectral simulations, can provide a route to determining  $T_{\text{rot}}$  in B<sub>2</sub>H<sub>6</sub>/CH<sub>4</sub>/Ar/H<sub>2</sub> plasmas. A more recent paper from the same group<sup>25</sup> reports first attempts at using OES to determine relative number densities of both B atoms and BH radicals in B<sub>2</sub>H<sub>6</sub>/CH<sub>4</sub>/Ar/H<sub>2</sub> plasmas, as functions of B/C ratio in the input gas mixture (in the range 0–0.02) and power density (in the range 9–23 W cm<sup>−3</sup>) and to explore some of the more important reaction kinetics. Specifically, the measured trends in B\* and BH\* emission intensities were compared to results obtained from a zero-dimensional (0D) kinetic model that followed previous suggestions<sup>24</sup> by assuming thermal decomposition of diborane (eq 1), and efficient interchange between the various BH<sub>x</sub> species via the sequence of H-shifting reactions, eqs 2–4,



but, in addition, invoked B/C coupling via reactions between BH<sub>x</sub> species ( $x \leq 1$ ) and C<sub>2</sub>H<sub>2</sub> as a possible rationale for marked differences between the observed and modeled trends in the [B]/[BH] ratio. Here we consider thermal dissociation (1) for M = B<sub>2</sub>H<sub>6</sub>, C<sub>2</sub>H<sub>2</sub>, and CH<sub>4</sub> assuming equal efficiencies (enhancement factors) for each of these partners. The rate coefficient  $k_1$  was derived and verified on the basis of available experimental data for the specific case of M = B<sub>2</sub>H<sub>6</sub>, (for details of this analysis and the complex multistage dissociation of diborane readers are referred to ref 32 and references within).

We have previously presented detailed two-dimensional (2D) modeling, absorption, and OES studies of MW activated CH<sub>4</sub>/Ar/H<sub>2</sub><sup>26–31</sup> and B<sub>2</sub>H<sub>6</sub>/Ar/H<sub>2</sub><sup>32</sup> plasmas. Here we report three mutually complementary strands of research that, when considered together with knowledge derived from previous studies of the respective three-element gas mixtures, offer an improved understanding of the more complex four-element B<sub>2</sub>H<sub>6</sub>/CH<sub>4</sub>/Ar/H<sub>2</sub> plasma under conditions relevant for B-doped diamond CVD. The new strands are, respectively: (i) absolute B and BH

column density measurements as functions of process condition (MW power,  $P$ ; total gas pressure,  $p$ ; and B<sub>2</sub>H<sub>6</sub>, CH<sub>4</sub>, and/or Ar input mole fractions) and height ( $z$ ) above the substrate surface; (ii) OES measurements of electronically excited BH, CH, and C<sub>2</sub> radicals, H<sub>2</sub> molecules, and H and Ar atoms, as functions of the same process conditions; and (iii) companion 2D modeling studies of the activation, gas-phase chemistry, and transport in such plasmas, focusing particularly on the following base conditions:  $p = 150$  Torr,  $P = 1.5$  kW, substrate temperature,  $T_{\text{sub}} = 973$  K, and flow rates  $F(\text{CH}_4) = 25$  standard cm<sup>3</sup> per minute (sccm),  $F(\text{Ar}) = 40$  sccm, and  $F(\text{H}_2) = 500$  sccm. The strands are presented in this order, with the latter providing explanations for (and being calibrated by) the experimental measurements in a synergistic fashion.

The present study serves to confirm the importance of reactions 1–4 in generating the mix of BH<sub>x</sub> ( $x \leq 3$ ) radicals within the CVD reactor, reveals marked differences in the spatial distributions of these radicals and in their respective variations with change in process conditions, and confirms the need for B/C coupling reactions within the overall kinetic scheme. The literature relating to gas phase B/C coupling reactions is limited, but the present analysis favors reactions between BH<sub>3</sub> radicals and unsaturated hydrocarbons such as C<sub>2</sub>H<sub>4</sub> and C<sub>2</sub>H<sub>2</sub> in the cooler periphery of the reactor as the most probable route for providing such coupling in B-doped diamond CVD environments. As in the earlier studies of B<sub>2</sub>H<sub>6</sub>/Ar/H<sub>2</sub> plasmas, effects attributable to the presence of traces of O<sub>2</sub> impurity are clearly discernible at low  $F(\text{CH}_4)$ .

## 2. Experimental Section

The experimental setup has been reported previously.<sup>27,29,30,32</sup> A small amount of dilute B<sub>2</sub>H<sub>6</sub>/H<sub>2</sub> mixture was added to an established Ar/H<sub>2</sub> plasma. Once the BH(A → X) emission signal at ~433.2 nm (monitored by a charge coupled device (CCD) detector mounted at the exit of a small monochromator) had become stable—typically >30 min after first introducing the B<sub>2</sub>H<sub>6</sub>—a flow of 25 sccm of CH<sub>4</sub> was added. CRDS and OES measurements typically commenced 15 min after the CH<sub>4</sub> addition. The BH and B column densities were then measured by CRDS as functions of  $P$ ,  $p$ ,  $F(\text{B}_2\text{H}_6)$ ,  $F(\text{CH}_4)$ , and  $F(\text{Ar})$ , as well as height above the substrate ( $z$ ). CRDS was also used to measure CH, C<sub>2</sub>(a), and H( $n = 2$ ) column densities as a function of  $F(\text{B}_2\text{H}_6)$  using appropriate dye laser wavelengths and CRDS mirror sets as detailed previously.<sup>29,32</sup>

“Base” conditions for the present CH<sub>4</sub>/B<sub>2</sub>H<sub>6</sub>/Ar/H<sub>2</sub> plasma studies were defined in the Introduction. As in our recent CRDS studies of MW activated B<sub>2</sub>H<sub>6</sub>/Ar/H<sub>2</sub> plasmas,<sup>32</sup> it was necessary to use different  $F(\text{B}_2\text{H}_6)$  values (0.003 sccm for the B atom measurements, and 0.009 sccm for the BH measurements) in order to avoid truncation of the measured B absorption lineshapes yet still ensure sufficient signal for BH detection. These B<sub>2</sub>H<sub>6</sub> flow rates correspond to input B/C ratios of  $2.4 \times 10^{-4}$  and  $7.2 \times 10^{-4}$ , respectively, that is, some 1–2 orders of magnitude lower than in the recently reported OES studies of Rayar et al.,<sup>25</sup> but sensibly in the range of process conditions relevant to most commercial B-doped diamond CVD. Again, as previously, when varying one discharge parameter, all others were maintained at their base values except when investigating the effects of changing  $F(\text{Ar})$ ,  $F(\text{B}_2\text{H}_6)$ , or  $F(\text{CH}_4)$ —where any variation away from the base total flow rate,  $F_{\text{total}} = 565$  sccm, was offset by a compensatory adjustment of  $F(\text{H}_2)$ .

## 3. Experimental Results and Discussion

**3.1. Emission and Absorption Spectra.** Figure 1 shows typical OE spectra measured in CH<sub>4</sub>/Ar/H<sub>2</sub> plasmas with and

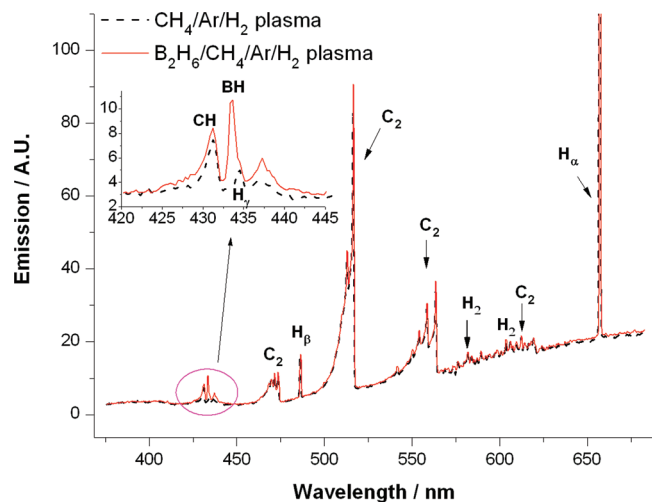


**Figure 1.** Optical emission spectra measured in  $\text{CH}_4/\text{Ar}/\text{H}_2$  and  $\text{B}_2\text{H}_6/\text{CH}_4/\text{Ar}/\text{H}_2$  plasmas under the same power ( $P = 1.5$  kW) and pressure ( $p = 150$  Torr) conditions, with  $F(\text{CH}_4) = 25$  sccm,  $F(\text{Ar}) = 40$  sccm, and  $F(\text{H}_2) = 500$  sccm together with, in the latter case,  $F(\text{B}_2\text{H}_6) = 0.05$  sccm (dashed and solid traces, respectively). The  $420 \leq \lambda \leq 445$  nm region is shown on an expanded scale (inset) to highlight the appearance of the BH(A-X) (0,0) Q branch in the latter spectrum.

without added  $\text{B}_2\text{H}_6$ . The two spectra are almost identical, apart from the feature at 433.2 nm associated with the BH(A  $\rightarrow$  X) (0,0) Q branch which is clearly evident in the magnified spectrum shown in the inset. The B( $3^2\text{S} \rightarrow 2^2\text{P}$ ) emission is also discernible in OE spectra recorded at shorter wavelengths ( $\sim 250$  nm) when  $\text{B}_2\text{H}_6$  is present in the gas mixture. The OES technique is renowned as a sensitive indicator of the plasma status. The striking consistency of the long wavelength parts of the two OES spectra shown in Figure 1 thus indicates that addition of trace amounts of  $\text{B}_2\text{H}_6$  has little effect on the overall chemistry occurring in a pre-established  $\text{CH}_4/\text{Ar}/\text{H}_2$  plasma. Such an observation should be contrasted with the cases of trace  $\text{B}_2\text{H}_6$  additions to an  $\text{Ar}/\text{H}_2$  plasma,<sup>32</sup> and of adding  $\text{CH}_4$  to a pre-existing  $\text{B}_2\text{H}_6/\text{Ar}/\text{H}_2$  plasma (see later, Figures 4 and 6), in both of which cases the additions cause very obvious changes in the plasma characteristics.

Figure 2(a) compares absorption spectra of MW activated  $\text{B}_2\text{H}_6/\text{CH}_4/\text{Ar}/\text{H}_2$  (top) and  $\text{CH}_4/\text{Ar}/\text{H}_2$  (bottom) plasmas measured, by CRDS, over the wavenumber range 23365–23455  $\text{cm}^{-1}$ . These serve to illustrate both the overlapping nature of the BH(A-X) and CH(A-X) transitions, and the ways in which the high spectral resolution afforded by laser spectroscopy methods allows identification of several uncontaminated lines associated with the BH radical. Careful inspection of the BH(A-X) (0,0) R branch reveals that the lines subdivide into three classes: noncontaminated (NC), lines that are partially contaminated by the CH(A-X) absorption (PC), and those that are totally contaminated (TC). Twelve R branch transitions in the wavenumber range 23 287–23 513  $\text{cm}^{-1}$  (each of which appears as a pair of lines, with relative intensities 4:1, associated with, respectively, the  $^{11}\text{BH}$  and  $^{10}\text{BH}$  isotopologues) were examined and classified in this way; the results are summarized in Table 1. Higher and lower J lines within the BH(A-X) (0,0) R branch are either too weak or totally overlapped by dense CH(A-X) structure. CH(A-X) (1,1) hot band absorptions are clearly recognizable in the measured spectra, but the corresponding BH(A-X) hot bands occur at longer wavelength (lower wavenumber) than investigated in the present work, for example, the (1,1) R branch lies at  $\tilde{\nu} < 23\,120$   $\text{cm}^{-1}$ .<sup>23</sup>

The method for determining the effective rotational temperature of the BH radicals in the viewing column has been

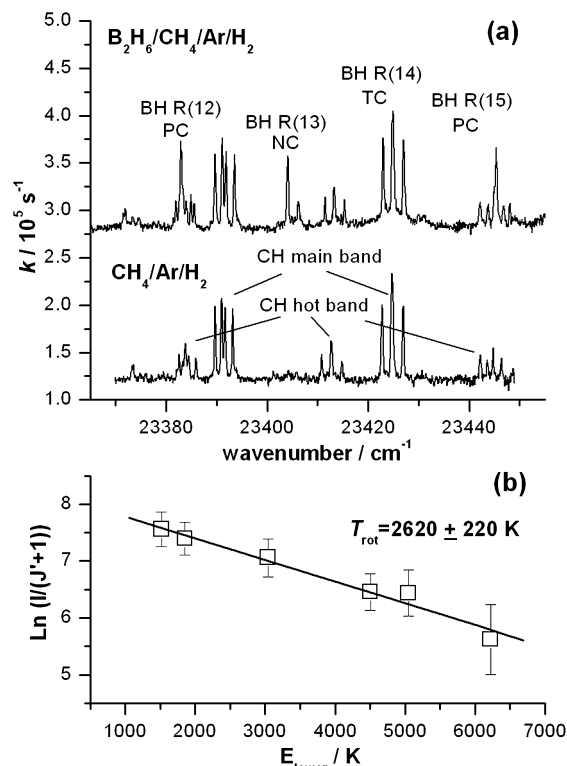


**Figure 2.** (a) Survey CRD spectra recorded (at  $z = 10$  mm) in the wavenumber range 23 365–23 455  $\text{cm}^{-1}$  for MW activated  $\text{CH}_4/\text{Ar}/\text{H}_2$  plasmas operating under base conditions with and without  $F(\text{B}_2\text{H}_6) = 0.025$  sccm (upper and lower traces, respectively). The individual BH(A  $\leftarrow$  X) lines in the upper trace are labeled as totally (TC), partially (PC) or noncontaminated (NC) by lines in the CH(A  $\leftarrow$  X) spectrum. (b) BH rotational temperature determined from a Boltzmann plot of the LIAs of several of the NC R branch transitions, measured under the latter conditions at  $z = 10$  mm.

**TABLE 1:  $^{11}\text{BH}(\text{A-X}, 0,0)$  R-Branch Lines, and the Extent of Their Contamination by Overlapping CH(A-X) Absorptions**

transition	wavenumber ( $\text{cm}^{-1}$ )	status*
R(8)	23 291.10	PC
R(9)	23 314.69	NC
R(10)	23 337.91	NC
R(11)	23 360.65	TC
R(12)	23 382.82	PC
R(13)	23 404.31	NC
R(14)	23 425.02	TC
R(15)	23 444.80	PC
R(16)	23 463.54	NC
R(17)	23 481.10	NC
R(18)	23 497.31	PC
R(19)	23 512.02	NC

\* NC: noncontaminated, PC: partially contaminated, TC: totally contaminated.

summarized elsewhere.<sup>32</sup> Figure 2b shows a Boltzmann plot derived from the line integrated absorbances (LIAs) of noncontaminated R branch lines of  $^{11}\text{BH}$  radicals measured at  $z = 10$  mm in a  $\text{B}_2\text{H}_6/\text{CH}_4/\text{Ar}/\text{H}_2$  plasma operating under base conditions. The  $T_{\text{rot}}$  value so derived ( $\sim 2600$  K) is significantly higher than that determined in an equivalent study of the  $^{11}\text{BH}$  radicals in a hydrocarbon-free  $\text{B}_2\text{H}_6/\text{Ar}/\text{H}_2$  plasma ( $\sim 2300$  K<sup>32</sup>). The method of calculating total B and BH column densities from the measured CRDS spectra was also described in the previous article.<sup>32</sup> Here, we choose the  $^{11}\text{BH}(\text{A-X})$  (0,0) R(10) line for all BH column density calculations. The PGOPHER



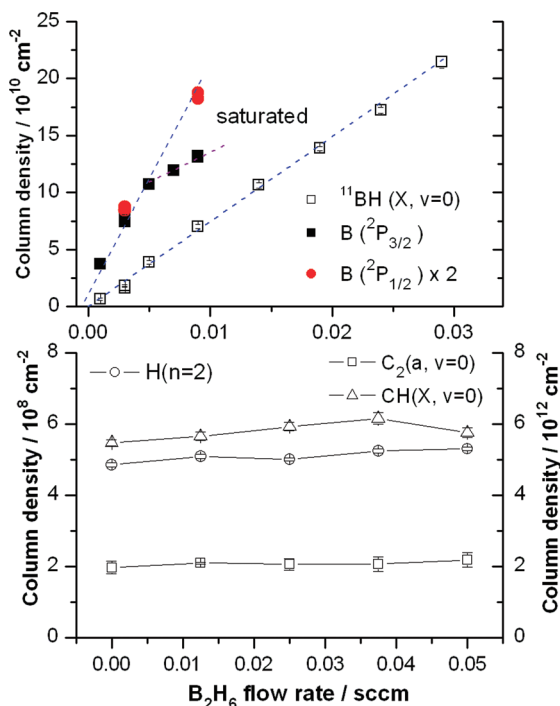


**Figure 3.** Column densities of (a)  $B(^2P_{3/2})$  atoms and  $^{11}BH(X, v=0)$  radicals, and (b)  $CH(X, v=0)$ ,  $C_2(a, v=0)$  radicals (right-hand axis) and  $H(n=2)$  atoms (left-hand axis) measured by CRDS at  $z = 10$  mm, as functions of  $F(B_2H_6)$ , with all other discharge parameters set at their base values. The  $B(3^2S_{1/2} \leftarrow 2^2P_{3/2})$  lineshapes showed clear evidence of truncation once  $F(B_2H_6) > 0.005$  sccm (■), but  $\{B(^2P_{3/2})\}$  values could still be estimated by monitoring the LIA of the weaker  $B(3^2S_{1/2} \leftarrow 2^2P_{1/2})$  transition, and multiplying its LIA by 2 (shown as ●). The displayed  $\{^{11}BH(X, v=0)\}$  values were derived from measurements of the LIA of the  $R(10)$  transition, and use of the appropriate PGOPHER coefficient<sup>33</sup> assuming  $T_{rot} = 2600$  K.

coefficient<sup>33</sup> for this line is relatively insensitive to temperature in the range  $1500 \leq T_{rot} \leq 3000$  K, and we therefore assume  $T_{rot} = 2600$  K for all BH column density calculations. As previously,<sup>32</sup> we use  $\{X\}$  and  $[X]$  to represent, respectively, the column density and the number density of a given species  $X$ , and scale the measured  $B(^2P_{3/2})$  and  $^{11}BH(v=0)$  column densities by factors of, respectively, 1.5 and 1.25 in order to derive  $\{B\}_{total}$  and  $\{BH(X, v=0)\}_{total}$ .

### 3.2. CRDS Measurements of B and BH Column Densities.

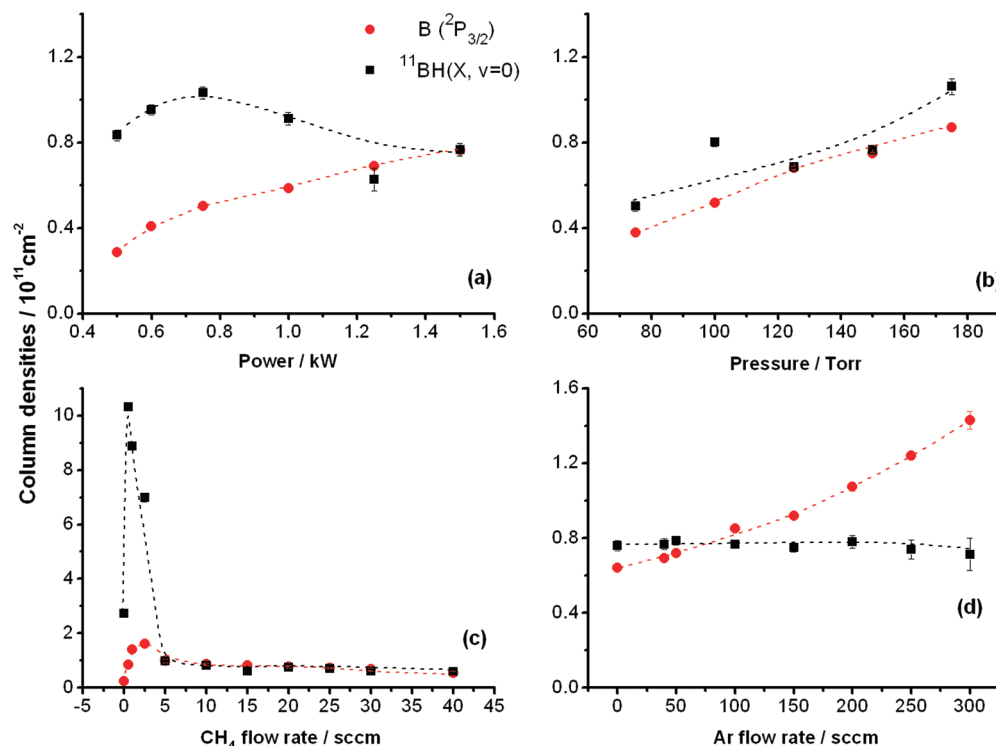
Figure 3a shows  $B(^2P_{3/2})$  and  $^{11}BH(X, v=0)$  column densities determined in the  $B_2H_6/CH_4/Ar/H_2$  plasma operating under base conditions, as a function of  $F(B_2H_6)$ . The B atom data at lowest  $F(B_2H_6)$  was obtained by CRDS measurements on the more intense  $B(3^2S_{1/2} \leftarrow 2^2P_{3/2})$  line at  $\tilde{\nu} = 40\,024.4$   $cm^{-1}$ , but, as Figure 3a shows, this spectral line shape began to “saturate” at  $F(B_2H_6) \sim 0.005$  sccm. Given the small spin–orbit splitting of the  $B(2^2P_J)$  state and the high gas temperature,  $\{B(^2P_{3/2})\}$  values at higher  $F(B_2H_6)$  could be estimated reliably by monitoring the weaker  $B(3^2S_{1/2} \leftarrow 2^2P_{1/2})$  transition at  $\tilde{\nu} = 40\,039.65$   $cm^{-1}$ , and multiplying its measured LIA by 2. The key finding from these measurements is that both  $\{B(^2P_{3/2})\}$  and  $\{^{11}BH(X, v=0)\}$  scale linearly with  $F(B_2H_6)$ , even at the lowest  $B_2H_6$  flow rates, in marked contrast to their nonlinear scaling in a  $B_2H_6/Ar/H_2$  plasma.<sup>32</sup> Such findings provide further evidence that the effect of any trace air contamination on the B and BH densities is greatly reduced when  $CH_4$  is present.  $\{C_2(a, v=0)\}$ ,  $\{CH(X, v=0)\}$ , and  $\{H(n=2)\}$  values determined under the same process conditions and at the same  $z$  (10 mm) are shown in Figure 3b. None of these column densities show any obvious variation with  $F(B_2H_6)$ , reinforcing the view that addition of a

small amount of  $B_2H_6$  has little impact on a pre-existing  $CH_4/Ar/H_2$  plasma.

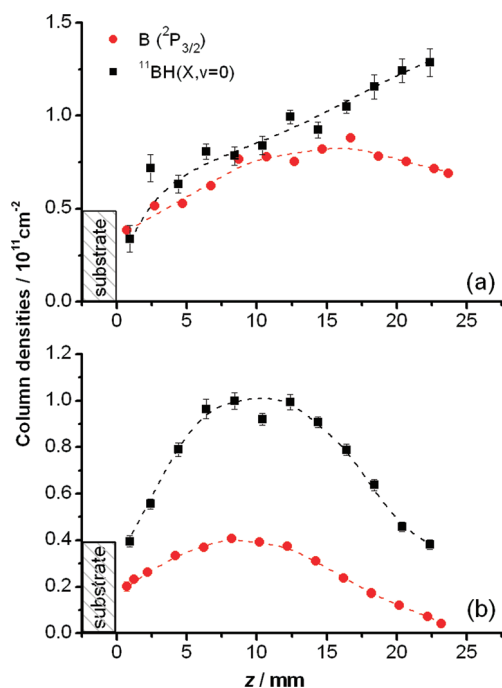
Figure 4 shows the measured (by CRDS, at  $z = 10$  mm) variation of  $\{B(^2P_{3/2})\}$  and  $\{^{11}BH(X, v=0)\}$  in the  $B_2H_6/CH_4/Ar/H_2$  plasma while varying (a)  $P$ , (b)  $p$ , (c)  $F(CH_4)$ , and (d)  $F(Ar)$ , with all other parameters held at their base values. Before discussing these data in turn, it is worth re-emphasizing two points. First, CRDS measurements return absorbances along a viewing column that spans an inhomogeneous distribution of  $T_{gas}$  and species mole fractions, which will vary in response to any significant change in process conditions. Some caution is therefore required when attempting to associate changes in measured absorbance with changes in local  $T_{gas}$  and species density within the reactor. Second, the B and BH densities in models of  $B_2H_6$  containing plasmas at pressures relevant to the present work are determined by thermal chemistry. Possible electron-induced contributions are thus (temporarily) ignored in the discussion that follows.

Figure 4a shows that  $\{B(^2P_{3/2})\}$  increases with  $P$ , whereas  $\{^{11}BH(X, v=0)\}$  first increases over the range  $0.5 \leq P \leq 0.7$  kW, then declines. The  $\{B\}_{total}/\{BH(X, v=0)\}_{total}$  ratio (derived from the measured  $B(^2P_{3/2})$  and  $^{11}BH(v=0)$  column densities as described in Section 3.1) increases steadily over the range  $0.5 \leq P \leq 1.5$  kW and is consistently larger than that measured in a  $B_2H_6/Ar/H_2$  plasma.<sup>32</sup> Increasing  $P$  can be expected to result in some expansion of the plasma volume, and increases in  $T_{gas}$ ,  $n_e$ , and  $[H(n=1)]$  in the plasma region;  $T_e$  is relatively insensitive to  $P$  (as shown previously,<sup>30,32</sup> and by the OES results reported in Section 3.3). The present observations can be understood, qualitatively, by assuming that the net rates of the H-shifting reactions 2–4 in the hot regions are faster than reactions between B- and C-containing species. The absolute  $[BH_x]$  densities are thus determined by the extent of  $B_2H_6$  decomposition ( $\sim 75$ – $80\%$ , from the difference between the input and calculated output  $B_2H_6$  diborane flow rates, and increasing with plasma volume), and the relative densities of  $[B]$  and  $[BH]$  by the equilibrium associated with reaction 4. Increasing  $T_{gas}$  and the plasma volume encourages  $B_2H_6$  and  $H_2$  decomposition. Reaction 4 is exothermic, so its equilibrium should shift to the left upon increasing  $T_{gas}$ , but increases in  $[H]$  as a result of increased  $H_2$  dissociation will have the opposite effect. The measured trends in  $\{B(^2P_{3/2})\}$  and  $\{^{11}BH(X, v=0)\}$  at the higher powers displayed in Figure 4(a) ( $P > 0.75$  kW) reflect the increasing plasma volume (and thus the increased column length probed at  $z = 10$  mm), and suggest that the  $T_{gas}$  induced increase in  $[H]$  has the greater influence on the respective column densities. We recognize, however, that the present CRDS measurements must also be sensitive to changes in the  $[BH]$  and  $[B]$  spatial distributions along the probed column. As shown later (Figure 5), the maxima of the  $\{B(^2P_{3/2})\}$  and  $\{^{11}BH(X, v=0)\}$  distributions both shift to smaller  $z$  (i.e., closer to the substrate) upon reducing  $P$ —reflecting the decreasing plasma volume. Thus, the present measurements probably sample the wings of these distributions more efficiently at high  $P$  but favor the cores of the distributions at low  $P$ .

Figure 4b shows that  $\{B(^2P_{3/2})\}$  and  $\{^{11}BH(X, v=0)\}$  both increase almost linearly with  $p$ . The  $\{B\}_{total}/\{BH(X, v=0)\}_{total}$  ratio remains roughly constant and, again, is significantly larger than found in corresponding measurements of the hydrocarbon-free  $B_2H_6/Ar/H_2$  plasma.<sup>32</sup> Higher  $p$  will result in a smaller plasma volume, a higher power density and thus higher  $T_{gas}$ ,  $[H]$ , and  $n_e$ , but reduced  $T_e$ . The observed trends in  $\{B(^2P_{3/2})\}$  and  $\{^{11}BH(X, v=0)\}$  suggest that neither column density is particularly sensitive to such changes and, as in the case of the



**Figure 4.** CRDS measured  $B(^2P_{3/2})$  and  $^{11}BH(X, v = 0)$  column densities (obtained by monitoring the R(10) line at  $z = 10$  mm), plotted as functions of (a)  $P$ ; (b)  $p$ ; (c)  $F(CH_4)$ , and (d)  $F(Ar)$ .  $F(B_2H_6) = 0.003$  and  $0.009$  sccm, respectively, and all other discharge parameters (apart from the one being varied) were maintained at their base values, apart from  $F(H_2)$ , which was adjusted to maintain  $F_{\text{total}} = 565$  sccm when varying  $F(CH_4)$  or  $F(Ar)$  away from their base values. The  $\{^{11}BH(X, v = 0)\}$  values have been calculated assuming  $T_{\text{rot}} = 2600$  K except for the point at  $F(CH_4) = 0$  in panel (c), where  $T_{\text{rot}} = 2300$  K is used.



**Figure 5.**  $B(^2P_{3/2})$  and  $^{11}BH(X, v = 0)$  column densities determined by CRDS under base discharge conditions with  $F(B_2H_6) = 0.003$  and  $0.009$  sccm, respectively, plotted as functions of  $z$  at  $P =$  (a)  $1.5$  kW and (b)  $0.6$  kW.

$B_2H_6/Ar/H_2$  plasma, the similar increases in  $\{B(^2P_{3/2})\}$  and  $\{^{11}BH(X, v = 0)\}$  are primarily determined by the increase in the total gas concentration as  $p$  is increased.

$\{B(^2P_{3/2})\}$  and  $\{^{11}BH(X, v = 0)\}$  show similar, but distinctive, variations with increase in  $F(CH_4)$ , as shown in Figure 4(c). At

low flow rates ( $0 < F(CH_4) < 5$  sccm), both increase rapidly, then fall. The optical emission from a  $B_2H_6/Ar/H_2$  plasma shows a weak purple halo, attributable to  $BH(A \rightarrow X)$  emission.<sup>32</sup> This halo becomes noticeably more distinct upon adding a small amount of  $CH_4$  to a pre-existing  $B_2H_6/Ar/H_2$  plasma, suggesting that small  $CH_4$  additions do not cause substantial changes in the plasma volume. Given the findings of our earlier study of  $B_2H_6/Ar/H_2$  plasmas,<sup>32</sup> it is tempting to suggest that the evident increase in  $\{B\}$  and  $\{BH\}$  at low  $F(CH_4)$  is attributable to some H/B/C/O conversion effects (associated with the presence of trace quantities of air), which is a point we return to in Section 4.2. Further addition of  $CH_4$  will tend both to getter any  $O_2$  impurity completely and to deplete  $[H]$  in the cooler regions, mitigating against B and BH generation by H-shifting reactions involving higher  $BH_x$  ( $x > 1$ ) species. Once  $F(CH_4) > 5$  sccm, both  $\{B(^2P_{3/2})\}$  and  $\{^{11}BH(X, v = 0)\}$  show a gradual decline with increasing  $F(CH_4)$ , and the  $\{B\}_{\text{total}}/\{BH(X, v = 0)\}_{\text{total}}$  ratio remains almost constant. The linear decrease in both B and BH column densities once  $F(CH_4) > 5$  sccm is likely attributable to B–C coupling reactions involving  $BH_x$  radicals and stable hydrocarbons. Previous modeling of  $CH_4/Ar/H_2$  plasmas in this same reactor shows that, at base conditions,  $[CH_4] > [C_2H_2]$  at  $r > 4$  cm, but that  $C_2H_2$  accounts for  $>97\%$  of the total carbon in the plasma ball itself.<sup>26,28</sup> The near constancy of the  $\{B\}_{\text{total}}/\{BH(X, v = 0)\}_{\text{total}}$  ratio supports the earlier assumption that the rates of the H-shifting reactions between the various  $BH_x$  species are fast compared with their net loss rates via such B–C coupling reactions.

Figure 4d shows that  $\{B(^2P_{3/2})\}$  more than doubles upon increasing  $F(Ar)$  from 0 to 300 sccm, while  $\{^{11}BH(X, v = 0)\}$  shows little change. These observations have obvious parallels with the corresponding variations with  $P$  (Figure 4a). Increasing  $F(Ar)$  necessarily reduces  $[H_2]$ . For a given input power, the

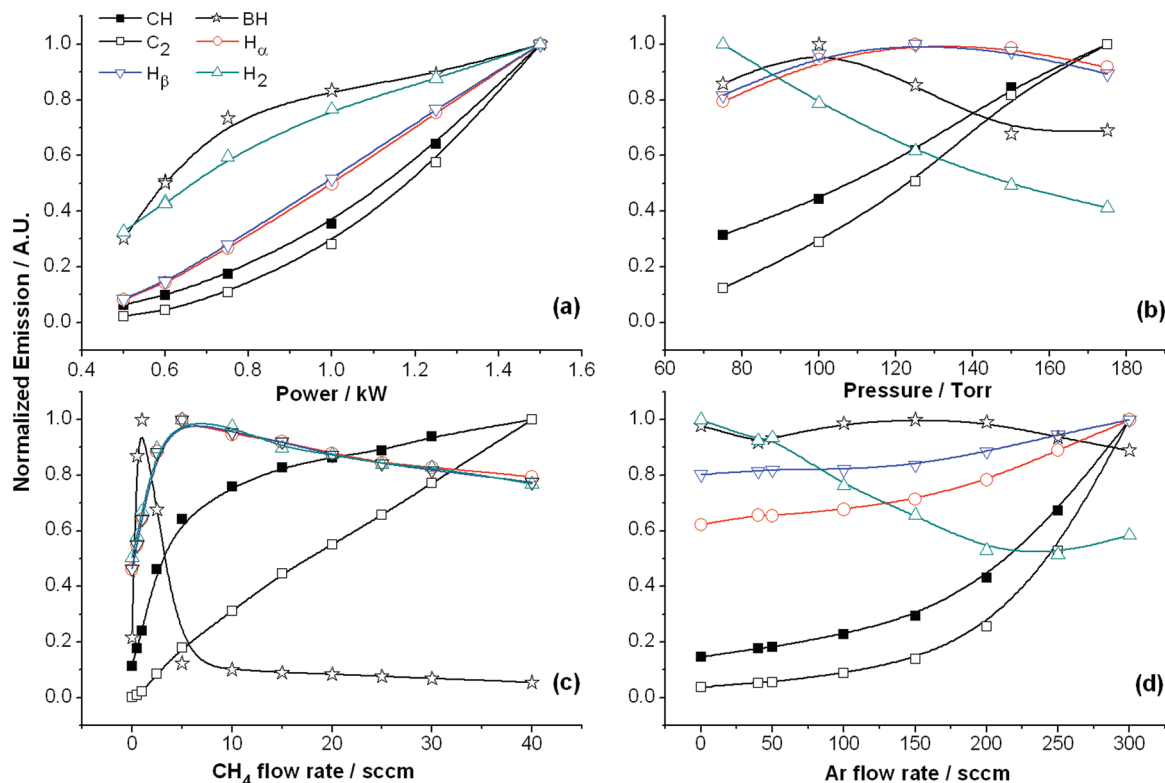


**Figure 6.** Normalized optical emission intensities of BH\*, CH\*, C<sub>2</sub>\*, H<sub>α</sub>, H<sub>β</sub>, and H<sub>2</sub>\* plotted as functions of (a)  $P$ ; (b)  $p$ ; (c)  $F(\text{CH}_4)$ , and (d)  $F(\text{Ar})$ . For these measurements,  $F(\text{B}_2\text{H}_6) = 0.009$  sccm and all other discharge parameters (apart from the one being varied) were held at their base values—apart from  $F(\text{H}_2)$ , which was adjusted to maintain  $F_{\text{total}} = 565$  sccm when varying  $F(\text{CH}_4)$  or  $F(\text{Ar})$  away from their base values.

power density therefore falls (since less electron energy can be accommodated in the form of H<sub>2</sub> rotational and vibrational excitation) and the hot plasma volume expands.<sup>26,34</sup> Plasma expansion largely compensates any increase in  $T_{\text{gas}}$  that might have been anticipated on account of the reduced thermal conductivity of an Ar-rich plasma, with the result that the maximum  $T_{\text{gas}}$  value remains roughly constant.<sup>32</sup> The expansion of the hot region, that is, the region in which thermal dissociation of B<sub>2</sub>H<sub>6</sub> is effective, is the dominant factor determining total {BH<sub>x</sub>}. The increase in {B(<sup>2</sup>P<sub>3/2</sub>)} (and in the {B}<sub>total</sub>/[{BH(X,  $\nu = 0$ )]<sub>total</sub> ratio) also reflects the increase in the hot plasma volume (i.e., the volume of high [H]), which shifts reaction 4 in favor of products.

Figure 5 shows the {B(<sup>2</sup>P<sub>3/2</sub>)} and {<sup>11</sup>BH(X,  $\nu = 0$ )} column densities measured by CRDS in a B<sub>2</sub>H<sub>6</sub>/CH<sub>4</sub>/Ar/H<sub>2</sub> plasma, as a function of  $z$ , at two different input powers,  $P =$  (a) 1.5 kW and (b) 0.6 kW. As with the hydrocarbon-free B<sub>2</sub>H<sub>6</sub>/Ar/H<sub>2</sub> plasma,<sup>32</sup> the spatial distributions of {<sup>11</sup>BH(X,  $\nu = 0$ )} and {B(<sup>2</sup>P<sub>3/2</sub>)} under base conditions are far more extensive than those of, say, the CH(X) or C<sub>2</sub>(a) radicals in a CH<sub>4</sub>/Ar/H<sub>2</sub> plasma operating in this reactor under the same  $P$  and  $p$  conditions<sup>29</sup>—reflecting the different  $T_{\text{gas}}$  and [H] dependencies of the H-shifting reactions involved in establishing local equilibrium within the BH<sub>x</sub> and CH<sub>x</sub> families. The {<sup>11</sup>BH(X,  $\nu = 0$ )} spatial distributions in Figure 5 are more extensive than those of {B(<sup>2</sup>P<sub>3/2</sub>)}, peaking at larger  $z$  under both  $P$  conditions studied. Again, such trends are explicable if [H] is the dominant factor determining the position of the equilibrium between BH and B. The spatial distribution of B atoms will then be determined by a convolution of the local [BH] and [H( $n = 1$ )] densities and, since the latter are maximal in the hottest regions of the plasma, the peak of the [B] distribution would be expected to appear nearer the substrate than that of [BH], consistent with observation. The obvious differences between the {B} and {BH}

profiles in a B<sub>2</sub>H<sub>6</sub>/Ar/H<sub>2</sub> plasma,<sup>32</sup> and those measured in the presence of  $F(\text{CH}_4) = 25$  sccm, reflect the depletion of [H] in the cooler regions (large  $z$ ) that occurs upon adding CH<sub>4</sub>. The peaks of the {B} and {BH} distributions both move to smaller  $z$  upon reducing  $P$ , consistent with the obvious shrinkage of the plasma volume, and thus of the associated  $T_{\text{gas}}$  and [H] distributions, at low  $P$ . Such variations are generally consistent with the competing effects of  $T_{\text{gas}}$  and [H] on the positions of the various equilibria involving BH<sub>x</sub> species (reactions 2–4), but any detailed interpretation of the measured trends in column density would require more detailed knowledge of the various number density distributions along the probed column, as functions of  $z$ .

**3.3. OES Measurements of BH\*, CH\*, C<sub>2</sub>\*, H<sub>2</sub>\*, H<sub>α</sub>, and H<sub>β</sub>.** Optical emission emanates from species in excited electronic states which, in the present experiments, are populated primarily by electron impact excitation. OES measurements can thus provide additional information relating to the properties of the electrons—notably  $n_e$  and  $T_e$ . Excited states monitored in the present study include BH(A), CH(A), C<sub>2</sub>(d), H<sub>α</sub>, and H<sub>β</sub> (i.e., H( $n = 3$ ) and H( $n = 4$ ), respectively), using spectral features and wavelengths reported elsewhere.<sup>30,32</sup>

Figure 6 displays measured BH\*, CH\*, C<sub>2</sub>\*, H<sub>2</sub>\*, H<sub>α</sub>, and H<sub>β</sub> emission intensities recorded under base conditions (with  $F(\text{B}_2\text{H}_6) = 0.009$  sccm), plotted as functions of  $P$ ,  $p$ ,  $F(\text{CH}_4)$ , and  $F(\text{Ar})$  and normalized so that the maximum intensity for each species in each plot is unity. As shown in Figure 6a, the normalized CH\* and C<sub>2</sub>\* emissions increase most steeply with increasing  $P$ , the normalized H<sub>α</sub> and H<sub>β</sub> emissions rise less steeply and show very similar behaviors, whereas the BH\* emission increases least. The CRDS measurements (Figure 4a) showed that {BH(X,  $\nu = 0$ )} declines with increasing  $P$ ; the gradual rise in BH\* emission intensity reflects the increase in  $n_e$  that accompanies the increase in  $P$ . The C<sub>2</sub>\* and CH\*



emissions also rise most steeply with increasing  $p$  (Figure 6b), while the  $H_\alpha$  and  $H_\beta$  emission intensity curves are relatively flat across the range  $75 \leq p \leq 180$  Torr. Very analogous trends were observed with a  $CH_4/Ar/H_2$  plasma in this same reactor—highlighting, again, the minimal perturbation of the plasma parameters as a result of adding a trace amount of  $B_2H_6$ . As before,<sup>30</sup> the faster-than-linear increases in  $C_2^*$  and  $CH^*$  intensities are attributable to the  $p$ -induced increase in  $T_{gas}$ , while the intersection of the  $H_\alpha$  and  $H_\beta$  intensity curves implies some reduction in  $T_e$  with increasing  $p$ . This decline in  $T_e$  accounts for the marked fall in  $H_2^*$  emission intensity in Figure 6b, despite the linear scaling of  $[H_2]$  with  $p$ , whereas the near constancy of the  $H_\alpha$  and  $H_\beta$  intensities reflects the competing effects of increased  $H(n=1)$  (as a result of increased  $p$  and  $T_{gas}$ ) offset by the reduced  $T_e$ . As Figure 4b showed, the  $BH(X, v=0)$  radical density increases gently with  $p$ , reflecting the complex and competing effects of the variations of  $T_{gas}$  and  $[H]$  distributions on  $[BH(X, v=0)]$ . The decline in  $T_e$  will reduce the electron impact excitation probability, however, thereby accounting for the discernible drop in  $BH^*$  emission intensity with increasing  $p$ .

The  $BH^*$  emission intensity shows a marked increase, then decreases, over the range  $0 < F(CH_4) < 5$  sccm, and continues to decline gently at  $F(CH_4) > 5$  sccm (Figure 6c), in a manner reminiscent of that found for  $\{BH(X, v=0)\}$  by CRDS (Figure 4c). Previous 2D modeling of the plasma chemistry in this MW PECVD reactor has shown that  $CH_4$  addition to a pre-existing  $Ar/H_2$  plasma causes some increase in both  $T_{gas}$  and  $T_e$  in the hot plasma region,<sup>30</sup> but the large (order of magnitude) variation in  $BH^*$  emission at low  $F(CH_4)$  cannot be explained simply by changes in  $T_e$  and/or  $T_{gas}$ . We caution that most of these measurements were made at times when the plasma was still converging to its steady state, despite waiting 15 min after each change in process conditions before starting the measurement. The  $F(CH_4)$  dependences of all other emissions shown in Figure 6c are very similar to those observed previously in a  $CH_4/Ar/H_2$  plasma, and have been discussed and rationalized elsewhere.<sup>30</sup>

Figure 6d shows that the normalized  $BH^*$  emission intensity changes little over the range  $0 \leq F(Ar) \leq 300$  sccm. The  $C_2^*$  and  $CH^*$  emissions both increase, consistent with previous conclusions that substituting Ar for  $H_2$  causes an increase in the hot plasma volume. The  $H_\alpha$  and  $H_\beta$  emission intensities both show only modest increases over this range, implying that  $T_e$ ,  $n_e$ , and the maximal  $T_{gas}$  must remain fairly constant across this range of  $F(Ar)$ . These trends differ markedly from that seen in OES studies of the hydrocarbon-free  $B_2H_6/Ar/H_2$  plasma<sup>32</sup> but, as with the corresponding column density measurements (Figure 4d), can be understood in terms of the increased plasma volume and  $T_{gas}$ -induced increase in H atom density. The fall in  $H_2^*$  emission is, in part, an inevitable consequence of the decrease in  $[H_2]$  as  $F(Ar)$  increases, but is exacerbated by reactions (and/or quenching) of  $H_2^*$  by Ar.<sup>32</sup> As Figure 7 shows, the  $BH^*$  emission intensity scales linearly with  $F(B_2H_6)$  in the range 0–0.03 sccm (in contrast to our previous observations with a hydrocarbon-free  $B/H/Ar$  plasma<sup>32</sup>). Such behavior is consistent with the earlier proposal that, under standard conditions,  $CH_4$  is an efficient getter for any trace  $O_2$  impurity in the process gas. The  $CH^*$ ,  $C_2^*$ ,  $H_2^*$ ,  $H_\alpha$ , and  $H_\beta$  emissions, in contrast, all appear immune to this change in  $F(B_2H_6)$ , reinforcing the view that trace additions of  $B_2H_6$  have negligible impact on the pre-established chemistry in a  $CH_4/Ar/H_2$  plasma.

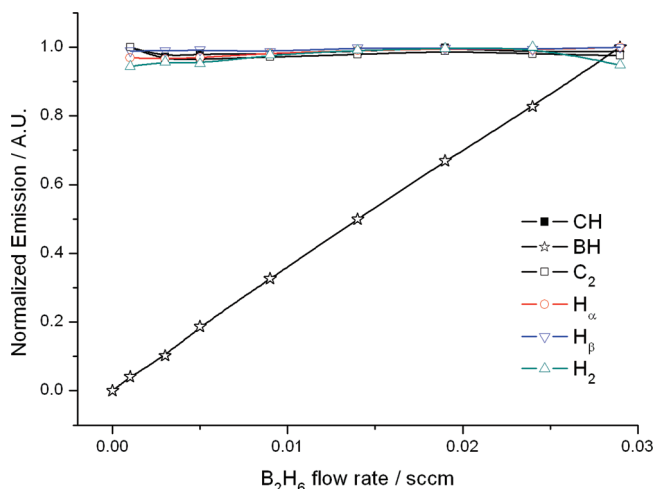


**Figure 7.** Normalized optical emission intensities of  $BH^*$ ,  $CH^*$ ,  $C_2^*$ ,  $H_\alpha$ ,  $H_\beta$ , and  $H_2^*$  measured under base conditions, plotted as a function of  $F(B_2H_6)$ .

#### 4. Modeling B/C/H/O/Ar Chemistry

All of the experimental data reported in this study indicates that addition of trace amounts of  $B_2H_6$  (at partial pressures relevant to most B-doped diamond CVD) causes little perturbation to the plasma chemistry prevailing in an existing  $CH_4/Ar/H_2$  plasma, which, for the present reactor, has been diagnosed and modeled extensively.<sup>26,28–30</sup> Such a finding is unsurprising, given that the B/C ratio in the input source gas is typically on the order of  $10^{-3}$ – $10^{-4}$ , and accords with the recent conclusions of Rayar et al.<sup>25</sup> The converse is not true, however; adding  $F(CH_4) = 25$  sccm causes major perturbation of a pre-existing  $B_2H_6/Ar/H_2$  plasma. We now seek to provide a quantitative rationale for the observed variations with changes in process condition described in the preceding section.

**4.1. B/H/O Chemical Mechanism.** Our recent extensive study of MW plasma activated  $B_2H_6/H_2/Ar$  mixtures<sup>32</sup> served to highlight the important effects of trace amounts of  $O_2$  impurity on the  $BH_x$  concentrations, as a result of  $BH_x$  conversion to more stable  $H_xB_yO_z$  species (e.g., HBO). Two distinct regimes were identified, experimentally and theoretically: the boron-deficient regime, (where  $F(B_2H_6) < F(O_2) \sim 0.006$  sccm under the prevailing experimental conditions) and the oxygen-deficient regime ( $F(B_2H_6) > F(O_2)$ ). In the former regime,  $BH_x$  is efficiently converted into  $H_xB_yO_z$  species, and the sum of the  $BH_x$  concentrations depends on diffusional transfer and the balance between the net rates of  $BH_x$  production (by thermal dissociation of  $B_2H_6$ ) and loss (predominantly via the reaction  $B + H_2O \rightarrow HBO + H$ ). In the second regime, most of the available oxygen is converted into  $H_xB_yO_z$  species like HBO, and the reduced  $H_2O$  density promotes a steeper increase of  $[BH_x]$  which further increases in  $F(B_2H_6)$ , with  $[BH_x] \sim (F(B_2H_6) - F(O_2))$ .<sup>32</sup>

**4.2. B/C/H/O Chemical Mechanism.** A coherent picture of the B/C/H chemical mechanism in both the high ( $T_{gas} \sim 1500$ – $3000$  K) and low ( $T_{gas} \sim 300$ – $1500$  K) gas temperature regions is still far from complete. Our previous publications provide details of the 2D model<sup>26</sup> and quantitative descriptions of the main plasma parameters and the spatially resolved gas temperature and species concentration distributions in  $H_2/Ar$ ,  $CH_4/H_2$ ,  $CH_4/H_2/Ar$ ,  $CH_4/H_2/He$  and  $B_2H_6/H_2/Ar$  gas mixtures.<sup>28–30,32,34,35</sup> One of the challenges of the present study is to determine the important reaction pathways (with known and/or assumed rate coefficients) in B/C/H gas mixtures containing trace amounts of  $O_2$  impurity.



However, this impurity is present at concentrations comparable with the typical B<sub>2</sub>H<sub>6</sub> flow rates, and we thus need to establish the much more complex, four component, B/C/H/O chemical mechanism that is consistent with the various experimental observations and measurements. The various BH<sub>x</sub> concentrations and their spatial distributions in a MW activated B/C/H/O gas mixture will depend upon the various chemical mechanisms (e.g., B/H, B/C, B/H/O, C/H/O), and the influence of the discharge processes and parameters (e.g., gas heating, the volume of plasma region, extent of H<sub>2</sub> dissociation, etc.) on the complex and, as yet, poorly established B/C/H/O chemistry.

As shown previously,<sup>32</sup> B atoms and BH radicals both display extensive spatial distributions in a B<sub>2</sub>H<sub>6</sub>/Ar/H<sub>2</sub> plasma operating under base conditions. Addition of CH<sub>4</sub> causes a marked increase in  $T_{\text{gas}}$  (and thus [H]) in the hot plasma region; for example, adding 4.4% CH<sub>4</sub> to a pre-existing 7%Ar/H<sub>2</sub> plasma is predicted to raise the maximum  $T_{\text{gas}}$  value from 2830 to 2930 K, and the H atom mole fraction,  $X_{\text{H}}$ , in the region of highest  $T_{\text{gas}}$  from ~5 to ~8%.<sup>26,28–30</sup> As shown in Section 3, CH<sub>4</sub> addition also causes some contraction of the spatial distributions of [B] and [BH], in both the radial and axial directions. The regimes identified in the previous analyses of B/H/O plasmas<sup>32</sup> are destroyed upon introducing significant amounts of CH<sub>4</sub>, and several new and important effects need to be recognized: (i) an additional stable species, CO, appears and competes with H<sub>x</sub>BO as a scavenger for any trace oxygen impurities; (ii) reaction with hydrocarbons could constitute an additional loss mechanism for BH<sub>x</sub> species, and stable H<sub>x</sub>B<sub>y</sub>C<sub>z</sub> products could be effective sinks for boron; and (iii) an indirect effect of adding CH<sub>4</sub> is the substantial (orders of magnitude) drop in H atom density in the cooler periphery of the reactor, as a result of H atom consumption in the CH<sub>4</sub> → C<sub>2</sub>H<sub>2</sub> conversion.<sup>23,28</sup> This reduces the spatial extent of the [B] and [BH] distributions, and the loss of boron to the reactor walls.

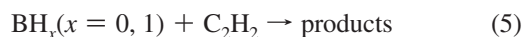
Our earlier modeling of hydrocarbon-free H/B/O plasmas<sup>32</sup> assumed a common wall loss probability ( $\gamma_{\text{wall}} = 0.1$ ) for all BH<sub>x</sub> species. Here, however, it is necessary to assume reduced  $\gamma_{\text{wall}}$  values for both BH<sub>3</sub> and B<sub>2</sub>H<sub>6</sub> (i.e.,  $\gamma_{\text{wall}} = 0.1$  for B, BH, and BH<sub>2</sub>,  $\gamma_{\text{wall}} = 0.00001$  for BH<sub>3</sub>, and  $\gamma_{\text{wall}} = 0$  for B<sub>2</sub>H<sub>6</sub>) in order to prevent the calculated rate of boron loss (as BH<sub>3</sub>) to the reactor walls at low  $F(\text{CH}_4)$  (~1–2 sccm) from becoming unphysically high (and contrary to experimental observation). With these  $\gamma_{\text{wall}}$  values, B atoms (of all the BH<sub>x</sub> species) are calculated to make the greatest contribution to material deposition at the wall, under all reactor regimes studied, and the relative contributions from BH, BH<sub>2</sub>, and BH<sub>3</sub> are minor for any assumed variations of  $\gamma_{\text{wall}}$  ( $0 < \gamma_{\text{wall}} < 1$ ), except in the case of very low  $F(\text{CH}_4)$  discussed above.

Given that exchange between stable oxygen and boron scavenger species will be limited, all of these processes could contribute to the various hysteresis effects observed in the present experiments, for example, the differing behavior of BH<sub>x</sub> species concentrations upon increasing/decreasing  $F(\text{B}_2\text{H}_6)$  and  $F(\text{CH}_4)$ , or upon the order in which B<sub>2</sub>H<sub>6</sub> and CH<sub>4</sub> are introduced into a pre-existing Ar/H<sub>2</sub> plasma. More detailed discussion of these issues appears later in this section.

Starting with the chemical mechanisms developed previously for C/H<sup>23</sup> and B/H/O<sup>32</sup> plasmas, adding relevant parts of the C/H/O mechanism from GRI-Mech<sup>36</sup> and guided by our calculated results for the CH<sub>4</sub>/H<sub>2</sub>/Ar and B<sub>2</sub>H<sub>6</sub>/H<sub>2</sub>/Ar (with trace O<sub>2</sub> impurity) base mixtures, we are now in a position to embark on a quantitative study of activated B<sub>2</sub>H<sub>6</sub>/CH<sub>4</sub>/H<sub>2</sub>/Ar (plus trace O<sub>2</sub>) mixtures. The B/C/H/O mechanism so developed involves ~435 direct and reverse reactions, for 61 neutral and charged

species. These include the 38 species appearing in the C/H/Ar plasma mechanism,<sup>26</sup> supplemented by selected H<sub>x</sub>B<sub>y</sub>O<sub>z</sub> (B<sub>2</sub>H<sub>6</sub>, BH<sub>3</sub>, BH<sub>2</sub>, BH, B, B<sup>+</sup>, HBO, H<sub>2</sub>BO, O<sub>2</sub>, O, OH, and H<sub>2</sub>O<sup>32</sup>), H<sub>x</sub>C<sub>y</sub>O<sub>z</sub> (CO, HCO, HCCO, H<sub>2</sub>CCO, H<sub>2</sub>CO, CH<sub>2</sub>OH, CH<sub>3</sub>OH, CH<sub>3</sub>O) and H<sub>x</sub>B<sub>y</sub>C<sub>z</sub>O<sub>z'</sub> (CH<sub>2</sub>CHBH<sub>x</sub> and CH<sub>3</sub>CH<sub>2</sub>BH<sub>x</sub> (with  $x = 0–2$ ), and H<sub>x</sub>COBH<sub>2</sub> ( $x \leq 3$ )) species. The most important reactions (in the context of BH<sub>x</sub> species) are listed in Table 2. The present analysis should be recognized as an initial, minimal H/B/C/O reaction mechanism; development of a more complete mechanism would require proper consideration of additional steps involving heavier H<sub>x</sub>B<sub>y</sub>C<sub>z</sub>O<sub>z'</sub> species and H/B/C/O coupling reactions. Inevitably, the number of uncertain reactions and unknown reaction rate coefficients must rise rapidly upon inclusion of such steps. At this stage, therefore, we have concentrated on exploring the extent to which the present limited H/B/C/O mechanism can provide satisfactory explanations for the trends observed experimentally.

**4.3. B–C Coupling Reactions.** Thermodynamic and kinetic data pertaining to reactions 1–4 still contains significant uncertainties,<sup>32</sup> but these are minor in comparison with the paucity of data relating to possible B–C coupling reactions. Rayar et al.<sup>25</sup> invoked a major role for reaction 5



in order to reconcile variations in B and BH densities with input MW power (deduced from OES measurements) with the results of a 0D chemical kinetic model. Their analysis required adoption of a high rate constant for net loss of BH<sub>x</sub> ( $k_5 > 10^{13} \text{ cm}^3 \text{ mol}^{-1} \text{ s}^{-1}$ , approaching the gas kinetic limit collision rate), which the authors recognized as a potential problem since the envisaged products (e.g., HBCC) were unlikely to be stable sink species under the high  $T_{\text{gas}}$  and [H] conditions prevailing in the hot plasma region.

Figure 4c showed that both {B(2<sup>2</sup>P<sub>3/2</sub>)} and {BH(X,  $v = 0$ )} decline slowly with increasing  $F(\text{CH}_4)$ , once  $F(\text{CH}_4) > 5$  sccm. There is now widespread recognition that C<sub>2</sub>H<sub>2</sub> will be the dominant hydrocarbon species in the hot plasma region.<sup>26,37</sup> Nonetheless, our previous diagnosis and modeling of B<sub>2</sub>H<sub>6</sub>/Ar/H<sub>2</sub> plasmas<sup>32</sup> clearly suggests that the increase in  $T_{\text{gas}}$  upon CH<sub>4</sub> addition should result in increased B<sub>2</sub>H<sub>6</sub> dissociation in the hotter regions, and greater B and BH densities than are observed experimentally. As pointed out in the earlier discussion of reaction 5, it is unlikely that any loss via B–C coupling will involve irreversible reactions. Rather, we look for temporary sinks that might attain significant steady-state concentrations in the cooler, low [H], peripheral regions of the reactor. The dominant BH<sub>x</sub> species in such regions is the BH<sub>3</sub> radical. BH<sub>3</sub> is not expected to react with CH<sub>4</sub> itself, but it is a strong electrophile with a penchant for adding to unsaturated hydrocarbons. As previously,<sup>24</sup> therefore, it is reasonable to suggest that reactions like



and, particularly,



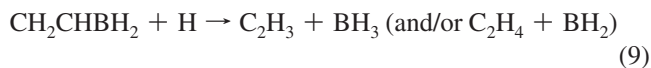
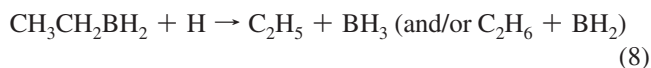
(with  $x = 1–3$ ), sequester some of the BH<sub>x</sub> radical density in both the hot (reaction 7) and cooler (reactions 6 and 7) regions of the reactor. Best current estimates for the reaction enthalpies

**TABLE 2: Kinetic Parameters for Some of the More Important B/C/H/O Coupling Reactions Implicated in the Modelling of B<sub>2</sub>H<sub>6</sub>/CH<sub>4</sub>/Ar/H<sub>2</sub> Plasmas Containing Trace O<sub>2</sub> Impurities<sup>a</sup>**

	reactions	<i>A</i> <sup>b</sup>	<i>B</i>	<i>E/R</i> (K)	ref
1	B <sub>2</sub> H <sub>6</sub> + M ↔ BH <sub>3</sub> + BH <sub>3</sub> + M, (M = B <sub>2</sub> H <sub>6</sub> , C <sub>2</sub> H <sub>2</sub> , CH <sub>4</sub> )	2.5 × 10 <sup>17</sup>	0	17 008	32
2	BH <sub>3</sub> + H ↔ BH <sub>2</sub> + H <sub>2</sub>	4.8 × 10 <sup>11</sup>	0.69	1211	23
3	BH <sub>2</sub> + H ↔ BH + H <sub>2</sub>	1.44 × 10 <sup>12</sup>	0.69	1211	23
4	BH + H ↔ B + H <sub>2</sub>	1.44 × 10 <sup>12</sup>	0.69	1211	23
5	B + H <sub>2</sub> O → HBO + H	2.4 × 10 <sup>14</sup>	0	1349	32
6	BH <sub>3</sub> + C <sub>2</sub> H <sub>4</sub> → CH <sub>3</sub> CH <sub>2</sub> BH <sub>2</sub>	3.1 × 10 <sup>13</sup>	0	0	<sup>c</sup>
7	BH <sub>3</sub> + C <sub>2</sub> H <sub>2</sub> → CH <sub>2</sub> CHBH <sub>2</sub>	1.55 × 10 <sup>13</sup>	0	0	<sup>c</sup>
6a	BH + C <sub>2</sub> H <sub>4</sub> → CH <sub>3</sub> CH <sub>2</sub> B	2.4 × 10 <sup>13</sup>	0	−252	40
7a	BH + C <sub>2</sub> H <sub>2</sub> → CH <sub>2</sub> CHB	1.2 × 10 <sup>13</sup>	0	−252	40
8	CH <sub>3</sub> CH <sub>2</sub> BH <sub>2</sub> + H → BH <sub>3</sub> + C <sub>2</sub> H <sub>5</sub> → BH <sub>2</sub> + C <sub>2</sub> H <sub>6</sub>	1.7 × 10 <sup>10</sup> 1.7 × 10 <sup>10</sup>	0 0	0 0	<sup>c</sup>
9	CH <sub>2</sub> CHBH <sub>2</sub> + H → BH <sub>3</sub> + C <sub>2</sub> H <sub>3</sub> → BH <sub>2</sub> + C <sub>2</sub> H <sub>4</sub>	1.7 × 10 <sup>10</sup> 1.7 × 10 <sup>10</sup>	0 0	0 0	<sup>c</sup>
10	HBO + H + M → H <sub>2</sub> BO + M				<sup>d</sup>
11	H + H <sub>2</sub> BO ↔ HBO + H <sub>2</sub>				<sup>d</sup>
12	H <sub>2</sub> BO + CH <sub>3</sub> + M → H <sub>3</sub> COBH <sub>2</sub> + M	5 × 10 <sup>18</sup>	0	0	<sup>b</sup>
13	H <sub>3</sub> COBH <sub>2</sub> + H(+M) → H <sub>3</sub> COBH <sub>3</sub> (+M)				<sup>e</sup>
14	H <sub>3</sub> COBH <sub>3</sub> + H → CH <sub>3</sub> OH + BH <sub>3</sub>	>3 × 10 <sup>13</sup>			<sup>f</sup>
15	CH <sub>3</sub> + H <sub>2</sub> BO → H <sub>2</sub> CO + BH <sub>3</sub>	10 <sup>10</sup>	0	9863	<sup>b</sup>
16	H <sub>y</sub> BO + CH <sub>x</sub> + M → H <sub>x</sub> COBH <sub>y</sub> + M (x < 3; y = 1, 2)	2 × 10 <sup>18</sup>	0	0	<sup>b</sup>
17	O + C <sub>2</sub> H <sub>2</sub> ↔ CO + CH <sub>2</sub>	6.94 × 10 <sup>6</sup>	2	956	36
18	OH + C <sub>2</sub> H <sub>2</sub> ↔ CO + CH <sub>3</sub>	4.83 × 10 <sup>−4</sup>	4	−1006	36
19	H + O <sub>2</sub> ↔ O + OH	2.65 × 10 <sup>16</sup>	−0.67	8575	36
20	O + H <sub>2</sub> ↔ H + OH	3.87 × 10 <sup>4</sup>	2.7	3150	36
21	OH + H <sub>2</sub> ↔ H + H <sub>2</sub> O	2.16 × 10 <sup>8</sup>	1.51	1726	36

<sup>a</sup> Rate constants are expressed in the traditional form:  $k[\text{cm}^3 \text{mol}^{-1} \text{s}^{-1}] = f(A, B, T) = AT^B \exp(-E/RT)$ . <sup>b</sup> Units of reaction coefficients are  $\text{cm}^3 \text{mol}^{-1} \text{s}^{-1}$  for two-body reactions and  $\text{cm}^6 \text{mol}^{-2} \text{s}^{-1}$  for three-body reactions. <sup>c</sup> Present study. <sup>d</sup> A constant  $[\text{H}_2\text{BO}]/([\text{HBO}] + [\text{H}_2\text{BO}])$  ratio of 0.1 is assumed as a result of reactions 10 and 11. <sup>e</sup> Pressure-dependent rate coefficient is used as for the reaction  $\text{H} + \text{C}_2\text{H}_5 (+\text{M}) \leftrightarrow \text{C}_2\text{H}_6 (+\text{M})$ .<sup>36</sup> The value of  $k_{13}(\text{M})$  under conditions of present relevance can be crudely approximated as  $k_{13}(\text{M}) \sim 9 \times 10^{11} \times T \times \exp(-0.0042 \times T) [\text{cm}^3 \text{mol}^{-1} \text{s}^{-1}]$  for  $500 \leq T \leq 2500 \text{ K}$ . <sup>f</sup> This reaction is assumed to be sufficiently fast to decompose most of the H<sub>3</sub>COBH<sub>3</sub> produced.

$\Delta_r H(6)$  and  $\Delta_r H(7)$  when  $x = 3$  are, respectively,  $-134 \text{ kJ mol}^{-1}$ <sup>38–40</sup> and  $-180 \text{ kJ mol}^{-1}$ .<sup>41</sup> Diode laser absorption studies of reaction 6 returned BH<sub>3</sub> removal rate constants  $>6 \times 10^{12} \text{ cm}^3 \text{mol}^{-1} \text{s}^{-1}$  at room temperature and N<sub>2</sub> buffer gas pressures as low as 6 Torr,<sup>42</sup> and flow-tube studies suggest that the adduct, ethylborane, is a major reaction product.<sup>43</sup> BH<sub>3</sub> addition to C<sub>2</sub>H<sub>2</sub> (reaction 7) has received little experimental attention but is a recognized route to forming vinylborane and is expected to show many similarities with reaction 6. We assume that H-shifting reactions within the CH<sub>3</sub>CH<sub>2</sub>BH<sub>x−1</sub> and CH<sub>2</sub>CHBH<sub>x−1</sub> families favor the more stable species—that is, ethylborane and vinylborane ( $x = 3$ ). Some of the presumed ethylborane and vinylborane products are likely to decompose through reactions with H atoms, i.e.,



that are expected to be, at most, mildly endothermic, and (to a lesser extent, because of the high energy barriers) by thermal

decomposition (reactions −6 and −7). In the context of BH<sub>x</sub> species, the detailed product branching is immaterial, given the efficiency of the H-shifting reactions 2–4. Some B–C adducts may be lost to the reactor walls, although the rate of material build-up on the walls with a B<sub>2</sub>H<sub>6</sub>/CH<sub>4</sub>/Ar/H<sub>2</sub> plasma under base conditions is noticeably less than that when operating the corresponding hydrocarbon-free plasma (where the calculated [B] distribution extends to the reactor walls<sup>32</sup>). Some B–C adducts will also presumably be exhausted through the base of the reactor. The present 2D calculations (below) show that C<sub>2</sub>H<sub>x</sub>BH<sub>2</sub> species are indeed formed (via reactions 6 and 7, Table 2) and accumulate in the cooler regions of the reactor from whence they diffuse to the hot plasma region and decompose via reactions 8 and 9.

**4.4. Local Maximum in {B} and {BH} at Low F(CH<sub>4</sub>) and the Effects of O<sub>2</sub>.** Extensive model calculations with the simple H/B/C/O reaction mechanism represented by eqs 1–9 in Table 2 failed to reproduce the prominent local maxima of {B}, {BH}, and BH\* observed experimentally at  $F(\text{CH}_4) \sim 1\text{--}2 \text{ sccm}$  (Figures 4c and 6c). Rather, these calculations suggested a gradual decline in the integral  $\{B(2^2P_{3/2})\}$  and  $\{BH(X, v = 0)\}$  profiles with increasing  $F(\text{CH}_4)$ , as a result of BH<sub>x</sub> conversion into CH<sub>2</sub>CHBH<sub>2</sub> and CH<sub>3</sub>CH<sub>2</sub>BH<sub>2</sub>. Conversely, if the BH<sub>x</sub> “sink” reactions 6–9 are omitted, the calculated B and BH column

densities show a systematic increase with increasing  $F(\text{CH}_4)$ , again without any local maximum at  $F(\text{CH}_4) \sim 1\text{--}2$  sccm. Three further possible explanations for the observed local maxima were considered:

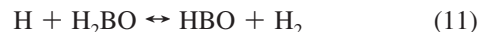
(i) Reduced B atom loss through reaction with  $\text{H}_2\text{O}$  (reaction 5), as a result of  $\text{H}_2\text{O}$  conversion to CO. This could impact positively on  $\{\text{BH}_x\}$  at low  $\text{C}_2\text{H}_2$  and  $\text{C}_2\text{H}_4$  concentrations (i.e., low  $F(\text{CH}_4)$ ) if, under such conditions, reactions 6–9 do not provide an effective sink for  $\text{BH}_x$  species. In this context, it is worth recalling the results of our previous IR absorption studies of  $\text{CH}_4/\text{H}_2/\text{Ar}$  plasmas in this same reactor, which showed that the  $\{\text{C}_2\text{H}_2\}/\{\text{CH}_4\}$  column density ratio increases by more than an order of magnitude as  $F(\text{CH}_4)$  is increased from 5 to 25 sccm.<sup>28</sup> The relative abundance of stable  $\text{C}_2\text{H}_x$  hydrocarbon species at yet lower  $F(\text{CH}_4)$  will be smaller still.

(ii) Unrecognized contributions from  $\text{NH}_x$  ( $x = 0\text{--}3$ ) species, which could be formed by electron impact dissociation of trace ( $\sim 40$  ppm) amounts of  $\text{N}_2$  present in the background air impurity. However, 0D calculations suggest that such dissociations, and subsequent H-shifting reactions, could only lead to steady-state  $\text{NH}_x$  species concentrations at the level of  $10^9\text{--}10^{10} \text{ cm}^{-3}$ .

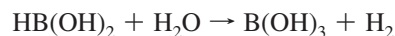
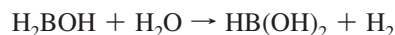
(iii) Enhanced  $\text{B}_2\text{H}_6$  dissociation efficiencies for  $\text{M} = \text{C}_x\text{H}_y$  species ( $\text{C}_2\text{H}_2$ ,  $\text{CH}_4$ , etc.) in reaction 1). As a result,  $[\text{B}_2\text{H}_6]$  in the hotter regions ( $T_{\text{gas}} > 1500 \text{ K}$ ) falls to negligible levels – in contrast to the case that  $\text{M} = \text{B}_2\text{H}_6$  is the only partner (as assumed for the  $\text{H}/\text{B}/\text{Ar}$  plasma<sup>32</sup>). In practice, however, the consequent change in the spatial distribution of the  $\text{B}_2\text{H}_6$  dissociation rate has little effect on the absolute values of the  $\{\text{BH}_x\}$  species or their spatial profiles.

None of these possible explanations succeeded in generating local maxima in the  $\{\text{B}\}$  and  $\{\text{BH}\}$  distributions at low  $F(\text{CH}_4)$ . Further consideration of possible alternative processes capable of providing a  $\sim 3\text{--}4$  fold increase of both B and BH concentrations upon introducing  $F(\text{CH}_4) = 1\text{--}2$  sccm – as observed experimentally – leads to the conclusion that  $\text{H}_x\text{B}_y\text{O}_z$  species are the only boron reservoir that could serve as the source for such an “explosion” of  $\text{BH}_x$  concentrations. Thus, we have sought an effective  $\text{H}_x\text{B}_y\text{O}_z \rightarrow \text{BH}_x$  conversion process, activated by the appearance of  $\text{C}_x\text{H}_y$  species. The overall conversion can be expected to involve two (or more) steps, via some  $\text{H}_x\text{B}_y\text{O}_z\text{C}_z'$  intermediate, given that  $\text{B}=\text{O}$  double bond cleavage is likely to involve a substantial energy barrier. We now present a more detailed analysis of the more abundant  $\text{H}_x\text{B}_y\text{O}_z$  and  $\text{H}_x\text{B}_y\text{O}_z\text{C}_z'$  species under the prevailing experimental conditions, and propose a plausible mechanism for  $\text{H}_x\text{B}_y\text{O}_z \rightarrow \text{H}_x\text{B}_y\text{O}_z\text{C}_z' \rightarrow \text{BH}_x$  conversion.

Our earlier studies of  $\text{B}_2\text{H}_6/\text{H}_2/\text{Ar}$  plasmas<sup>32</sup> demonstrated the existence of a B-containing sink species that, for simplicity, we treated as HBO. HBO is of course just one of a family of  $\text{H}_x\text{B}_y\text{O}_z$  species, but more detailed consideration of the distribution of  $\text{H}_x\text{B}_y\text{O}_z$  species was unnecessary since we assumed no reconversion to  $\text{BH}_x$  species (i.e., no  $\text{H}_x\text{B}_y\text{O}_z \rightarrow \text{BH}_x$  conversion in  $\text{B}/\text{H}/\text{O}$  mixtures). More detailed consideration of the thermochemical data for such species and of possible hydrogen activated chemical reaction mechanisms suggests that several  $\text{H}_x\text{B}_y\text{O}_z$  species might be important in  $\text{B}/\text{H}/\text{O}$  mixtures under the prevailing process conditions (i.e.,  $T_{\text{gas}} \sim 300\text{--}3000 \text{ K}$ , and  $X_{\text{H}} \leq 0.1$ ), including BO, HBO,  $\text{H}_2\text{BO}$ ,  $\text{H}_2\text{BOH}$ ,  $\text{HB}(\text{OH})_2$ , and  $\text{B}(\text{OH})_3$ . The local partitioning between the various  $\text{H}_x\text{B}_y\text{O}_z$  concentrations via reactions like

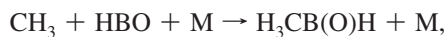


as well as  $\text{BO} + \text{H}_2 \leftrightarrow \text{HBO} + \text{H}$ ,  $\text{H}_2\text{BO} + \text{H} (+\text{M}) \leftrightarrow \text{H}_2\text{BOH} (+\text{M})$ ,  $\text{H}_2\text{BO} + \text{H}_2 \leftrightarrow \text{H} + \text{H}_2\text{BOH}$ , etc., will depend, in a complex manner, on the local  $T_{\text{gas}}$ , the  $\text{H}/\text{H}_2$  ratio, the  $\text{H}_x\text{O}_y$  concentrations, the diffusional fluxes of these various species, and the rates of the many reactions between them.<sup>44–47</sup> The more stable  $\text{H}_x\text{B}_y\text{O}_z$  species such as  $\text{HB}(\text{OH})_2$  and  $\text{B}(\text{OH})_3$  could be produced by reactions with  $\text{H}_2\text{O}$ ,<sup>48,49</sup> for example,



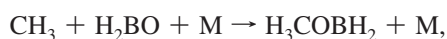
Reactions 10 and 11 appear to be important  $\text{H}_2\text{BO}$  production/loss reactions. Chin et al.<sup>47</sup> estimate the rate constant of reaction 10 in the high pressure limit to be quite high ( $k_{10}[\text{M}] > \sim 3 \times 10^{13} \text{ cm}^3 \text{ mol}^{-1} \text{ s}^{-1}$ ). That being the case, the  $\text{H}_2\text{BO}$  concentration (relative to that of HBO) may not be negligible, which is potentially important since, as we show below,  $\text{H}_2\text{BO}$  species could drive  $\text{H}_x\text{B}_y\text{O}_z \rightarrow \text{H}_x\text{B}_y\text{O}_z\text{C}_z' \rightarrow \text{BH}_x$  conversion.

Upon adding  $\text{CH}_4$ , some of the  $\text{H}_x\text{B}_y\text{O}_z$  species can be expected to react with  $\text{C}_x\text{H}_y$  species. We can envisage several possible  $\text{H}_x\text{B}_y\text{O}_z\text{C}_z'$  intermediates (and many possible reactions) that could contribute to the required  $\text{H}_x\text{B}_y\text{O}_z \rightarrow \text{H}_x\text{B}_y\text{O}_z\text{C}_z' \rightarrow \text{BH}_x$  conversion activated by  $\text{CH}_x$  species. In assessing the likely importance of such reactions we are guided by the available thermochemical data,<sup>32,50</sup> supplemented as and when required by the results of density functional theory (DFT) calculations. Potential energy minima and transition states associated with the various target reactions were fully optimized using the standard B3LYP functional together with the 6-31G\* basis set within the Gaussian 03 program.<sup>51</sup> Vibrational frequencies were computed to confirm the nature of all stationary points. Single-point B3LYP energies were then computed at the B3LYP/6-31G\* geometries using the larger 6-311+G(2df,p) basis. Any reported transition state energies ( $E_{\text{TS}}$ ) and reaction enthalpies ( $\Delta_r H$ ) are based on B3LYP/6-311+G(2df,p) energies with the B3LYP/6-31G\* geometries and zero-point energy corrections.  $\text{CH}_3$  and HBO are likely to be the most abundant  $\text{CH}_x$  and  $\text{H}_x\text{B}_y\text{O}_z$  radical species under the present experimental conditions. The DFT calculations suggest that the dominant reaction between these two species involves C–B bond formation



$$\Delta_r H = -64.5 \text{ kJ mol}^{-1}$$

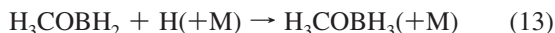
but, even when we consider subsequent reaction with H atoms, provides no obvious route for transferring the O from the B atom in the  $\text{H}_3\text{CB}(\text{O})\text{H}$  adduct as required in order to liberate  $\text{BH}_x$ . The alternative C–O bond forming channel (yielding  $\text{H}_3\text{COBH}$ ) is calculated to be endothermic, by  $\sim 52 \text{ kJ mol}^{-1}$ , and to have an activation barrier of  $\sim 111 \text{ kJ mol}^{-1}$ . A more feasible mechanism for  $\text{H}_x\text{B}_y\text{O}_z \rightarrow \text{H}_x\text{B}_y\text{O}_z\text{C}_z' \rightarrow \text{BH}_x$  conversion can be realized by starting with  $\text{H}_2\text{BO}$  rather than HBO, i.e. starting with the radical–radical addition



$$\Delta_r H = -318 \text{ kJ mol}^{-1} \quad (12)$$



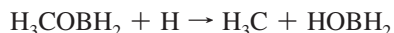
and then invoking further reactions with H atoms:



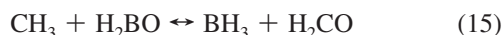
and



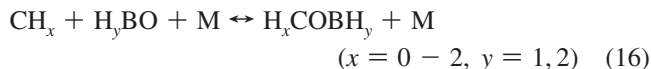
to restore  $\text{BH}_3$ . All steps in the mechanism 12–14 are calculated to be exothermic and essentially barrierless, but we recognize the existence of another exothermic pathway that can compete with reaction 13, i.e.,



which constitutes a null cycle as far as the required transfer of the O from B to C is concerned. Reaction 15,



a rival to reaction 12, is also exothermic, and could (in principle) provide an additional means of recovering  $\text{BH}_x$  species, but we anticipate that this reaction will not be important under the present experimental conditions (i.e., the energy barrier to forming these products is prohibitive in the cooler regions  $T_{\text{gas}} < 1000$  K). Analogues of reaction 12, reactions involving  $\text{CH}_x$  ( $x = 0-2$ ) species, i.e.,



and subsequent H additions can be expected to convert other  $\text{H}_x\text{COBH}_y$  species to the more stable and (under the present experimental conditions) more abundant  $\text{H}_3\text{COBH}_2$  (methoxyborane) species. We note that  $\text{H}_3\text{COBH}_2$  has been observed (and characterized) by microwave spectroscopy in both  $\text{B}_2\text{H}_6/\text{CH}_3\text{OH}$  and  $\text{B}_2\text{H}_6/\text{CH}_2\text{O}$  gas mixtures flowing through a quartz tube heated to  $\sim 600-700$  K.<sup>52</sup>

The  $\text{H}_2\text{BO}$  concentration in the present work is not well-known but, as mentioned above, may well be non-negligible (relative to that of  $\text{HBO}$ ). Lacking reliable rate data, we have performed 2-D model calculations incorporating reactions 10–16 to probe the feasibility of the proposed  $\text{H}_x\text{B}_y\text{O}_z \rightarrow \text{H}_x\text{B}_y\text{O}_z\text{C}_z \rightarrow \text{BH}_x$  conversion, assuming a constant  $[\text{H}_2\text{BO}]/([\text{HBO}] + [\text{H}_2\text{BO}])$  ratio of 0.1 (as a result of reactions 10 and 11). We have also assumed rate coefficients for reactions 12 and 16 that are typical for three-body reactions:  $k_{12} = 5 \times 10^{18} \text{ cm}^6 \text{ mol}^{-1} \text{ s}^{-1}$  and  $k_{16} = 2 \times 10^{18} \text{ cm}^6 \text{ mol}^{-1} \text{ s}^{-1}$  (Table 2), and that all of the  $\text{H}_3\text{COBH}_3$  adduct decomposes by reaction 14. For reaction 13, we have employed the same rate coefficients as for the reaction  $\text{H} + \text{C}_2\text{H}_5(+\text{M}) \leftrightarrow \text{C}_2\text{H}_6(+\text{M})$ .<sup>36</sup>

Given the lack of reliable kinetic data we have not considered other possible intermediates and products, for example,  $\text{H}_2\text{CBHOH}$ ,  $\text{HBCCH}_2$ , for which dissociation pathways to  $\text{BH}_x$  products seem improbable. Of course, in the assumed reduced reaction scheme (eqs 1–16), the rate coefficients, the participating  $\text{H}_x\text{B}_y\text{O}_z\text{C}_z$  species, and other as yet unrecognized steps within the full H/B/C/O mechanism all require further study and require reliable kinetic data. Nonetheless, the proposed reaction mechanism (Table 2) turns out to capture the observed H/B/C/O coupling processes. As demonstrated below, incorporation of

this mechanism within the 2D model has allowed us to reproduce the experimental trends observed under base conditions qualitatively, and quantitatively - even the local maximum in  $\{\text{B}\}$  and  $\{\text{BH}\}$  at  $F(\text{CH}_4) \sim 1$  sccm.

**4.5. 2D Model Results.** Most model outputs presented in this section assume the following base parameters:  $p = 150$  Torr,  $P = 1.5$  kW,  $T_{\text{sub}} = 973$  K,  $F(\text{Ar}) = 40$  sccm,  $F(\text{CH}_4) = 25$  sccm,  $F(\text{B}_2\text{H}_6) = 0.009$  sccm,  $F(\text{O}_2) = 0.006$  sccm (the typical  $\text{O}_2$  impurity level  $\sim 10$  ppm established in ref 32), and  $F(\text{H}_2) = 500$  sccm. Calculations were also carried out using one lower  $\text{B}_2\text{H}_6$  flow rate ( $F(\text{B}_2\text{H}_6) = 0.003$  sccm) and a range of  $F(\text{CH}_4)$  values (0, 1, 5, and 25 sccm); in the latter calculations,  $F(\text{H}_2)$  was adjusted in a compensatory manner such that  $F_{\text{total}} = 565$  sccm. We have focused particularly on trying to mimic the experimental results shown in Figures 4c and 6c, that is, the progressive addition of  $\text{CH}_4$  to an existing B/H/Ar/(O) plasma. In practice, the process gases are admitted into the reactor through two diametrically opposed 1/4" stainless steel pipes located close beneath the quartz window, but the modeling necessarily assumes cylindrical symmetry. The two local sources at  $r \sim 6$  cm were thus replaced by an annular source at the top of the reactor ( $R - dr < r < R$ , where  $R = 6$  cm and  $dr = 0.128$  cm are the chamber radius and the radial cell size, respectively), and the input flow reduced to ensure the experimental value of  $F_{\text{total}}$ . Further model calculations, that assumed a single source with cross-section equivalent to that in the experiment (i.e.,  $\sim 0.9$  cm in diameter, located centrally at the top of the reactor,  $0 < r < 0.45$  cm), returned somewhat different spatial distributions of species in the cold regions (especially for the primary species  $\text{B}_2\text{H}_6$ ,  $\text{CH}_4$ , and  $\text{O}_2$ ), but the species concentrations in the hot plasma region are generally immune to the choice of model by which gas is admitted to the reactor.

Figure 8 shows 2D( $r, z$ ) false color plots of the calculated B, BH,  $\text{BH}_2$ ,  $\text{BH}_3$ ,  $\text{B}_2\text{H}_6$ , and  $\text{CH}_2\text{CHBH}_2$  number density distributions for the base conditions (with the radial,  $r$ , axis directed horizontally and the axial  $z$ -axis directed vertically, and ( $r = 0, z = 0$ ) defining the center of the substrate surface). 2D distributions of  $T_{\text{gas}}$  and other key species concentrations (e.g., H,  $\text{CH}_x$ ,  $\text{C}_2\text{H}_2$  and electrons) for very similar operating conditions but without the addition of  $\text{B}_2\text{H}_6$  were reported in ref 26. The plots in Figure 8 serve to illustrate the progressive conversion of  $\text{B}_2\text{H}_6$  to  $\text{BH}_3$  and then to the smaller  $\text{BH}_x$  species, as well as the build up of stable B/C adducts in the cooler periphery regions. The plasma-chemical modeling predicts that the rate of the primary source of  $\text{BH}_x$  species (the thermal dissociation of diborane diffusing from the cold regions to the hot plasma region) maximizes in a thin layer centered at  $r \sim 5$  cm, where  $T_{\text{gas}} \sim 1000-1100$  K.

Figure 9 shows the calculated  $r$  distributions of  $T_{\text{gas}}$  and of the concentrations of selected species at  $z = 9.5$  mm for  $F(\text{CH}_4) = 1$  sccm (a) and 25 sccm (b), and just above the substrate ( $z = 0.5$  mm) for  $F(\text{CH}_4) = 25$  sccm (c). These calculations successfully reproduce the experimentally observed reduction of the  $[\text{H}]$ ,  $[\text{B}]$ , and  $[\text{BH}]$  radial profiles with increasing  $F(\text{CH}_4)$ . The reduced spatial extent of these profiles necessarily results in an increase of the calculated "effective" rotational temperature of the BH radicals (i.e., the density weighted temperature, averaged over the entire viewing column):  $T_{\text{rot}} \sim 2500$  K for  $F(\text{CH}_4) = 1$  sccm and  $T_{\text{rot}} \sim 2870$  K for  $F(\text{CH}_4) = 25$  sccm—c.f. the experimentally determined values  $T_{\text{rot}} \sim 2300$  K for  $F(\text{CH}_4) \leq 1$  sccm and  $T_{\text{rot}} \sim 2600$  K for  $F(\text{CH}_4) = 25$  sccm. The present modeling shows the  $\text{BH}_x$  concentrations to be relatively immune to the efficiencies of different M species in reaction 1. In total,  $\sim 75-80\%$  of the input  $\text{B}_2\text{H}_6$  molecules are found to be



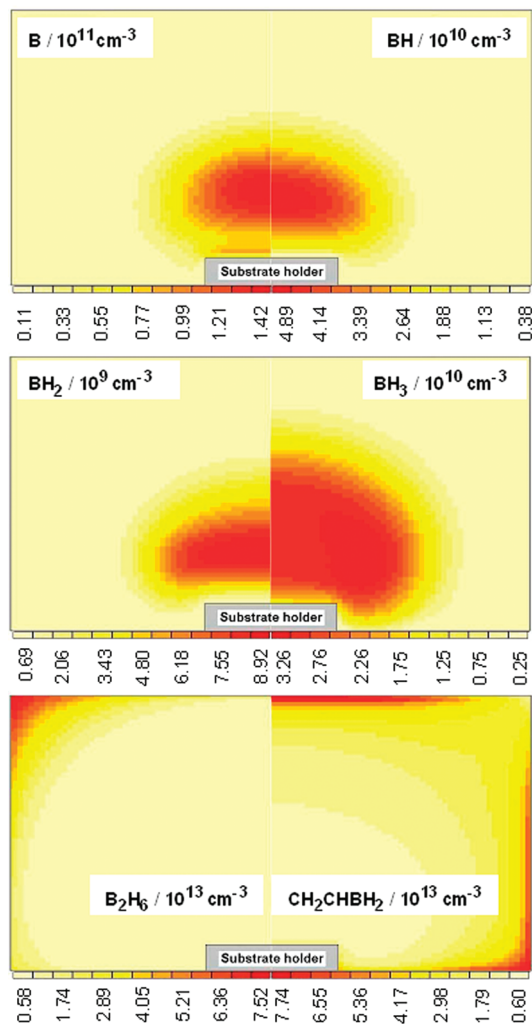


**Figure 8.** 2D( $r, z$ ) false color plots showing calculated distributions of B, BH, BH<sub>2</sub>, BH<sub>3</sub>, B<sub>2</sub>H<sub>6</sub>, and CH<sub>2</sub>CHBH<sub>2</sub> number densities under base conditions:  $P = 1.5$  kW,  $p = 150$  Torr,  $F(\text{H}_2) = 525$  sccm,  $F(\text{Ar}) = 40$  sccm,  $F(\text{CH}_4) = 25$  sccm,  $F(\text{B}_2\text{H}_6) = 0.009$  sccm, and  $F(\text{O}_2) = 0.006$  sccm.

dissociated, irrespective of whether we assume: (i) complete dissociation of B<sub>2</sub>H<sub>6</sub> in the hotter regions ( $T_{\text{gas}} > 1500$  K, with  $M = \text{B}_2\text{H}_6$ , C<sub>2</sub>H<sub>2</sub>, and CH<sub>4</sub>, as in earlier assumptions<sup>25</sup>); or (ii) that [B<sub>2</sub>H<sub>6</sub>] in the hot plasma region is nonzero and comparable to that of the lighter BH<sub>*x*</sub> species (i.e., as in case that  $M = \text{B}_2\text{H}_6$  only<sup>32</sup>). The CH<sub>3</sub>CH<sub>2</sub>BH<sub>2</sub> number density is much lower than that of CH<sub>2</sub>CHBH<sub>2</sub> (by factors of  $\sim 10^3$  in the hotter regions and  $\sim 3$  in the cool regions proximate to the reactor walls) and is thus not included in Figure 9. As Figure 9 also shows, the trace O<sub>2</sub> impurity is now shared between CO, H<sub>2</sub>O, H<sub>2</sub>BO (with an assumed partitioning of 10% H<sub>2</sub>BO, 90% HBO), and H<sub>3</sub>COBH<sub>2</sub>, and the effects of oxygen impurities on [BH<sub>*x*</sub>] are substantially reduced upon progressive addition of CH<sub>4</sub>.

Figure 10 shows the calculated  $z$ -dependence of the {B(2<sup>2</sup>P<sub>3/2</sub>)} and {BH( $X, v = 0$ )} distributions. These serve to illustrate the way both column densities decrease (in size and in absolute value) with increasing  $F(\text{CH}_4)$ . The model predictions for  $F(\text{CH}_4) = 25$  sccm are in quantitative accord with the absolute values of the  $z$ -dependent {B(2<sup>2</sup>P<sub>3/2</sub>)} and {BH( $X, v = 0$ )} profiles measured by CRDS at, respectively,  $F(\text{B}_2\text{H}_6) = 0.003$  and  $0.009$  sccm. As Figure 10c shows, the model calculations also succeed in reproducing the local maxima of {B}, {BH} and BH\* observed experimentally at  $F(\text{CH}_4) \sim 1$ – $2$  sccm (c.f. Figures 4c and 6c).

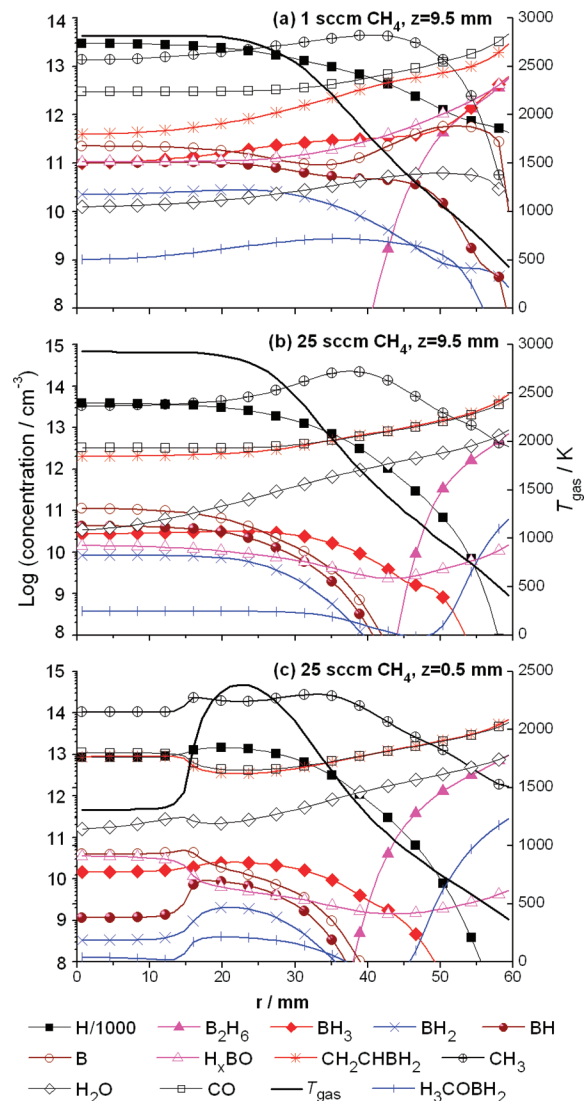


**Figure 9.** Radial distributions of  $T_{\text{gas}}$  (right-hand axis), the H, B, BH, BH<sub>2</sub>, BH<sub>3</sub>, B<sub>2</sub>H<sub>6</sub>, HBO, CH<sub>3</sub>, CH<sub>2</sub>CHBH<sub>2</sub>, H<sub>3</sub>COBH<sub>2</sub>, H<sub>2</sub>O, and CO number densities (in cm<sup>-3</sup>, left-hand axis) calculated for base conditions and  $F(\text{B}_2\text{H}_6) = 0.009$  sccm, at (a)  $z = 9.5$  mm,  $F(\text{CH}_4) = 1$  sccm, (b)  $z = 9.5$  mm,  $F(\text{CH}_4) = 25$  sccm, and (c)  $z = 0.5$  mm,  $F(\text{CH}_4) = 25$  sccm.

**4.6. B Incorporation Efficiencies.** Figure 9c showed that B atoms and BH<sub>3</sub> radicals are the most abundant BH<sub>*x*</sub> species in the vicinity of the growing diamond surface. Previous gas-surface modeling studies<sup>17</sup> returned such a low binding energy for BH<sub>3</sub> to a radical site on the diamond (100) surface that we discount BH<sub>3</sub> as an important species for accommodating B into the growing material, and henceforth focus attention on the incident B atoms. Figure 9c also allows us to compare the efficiency of boron and carbon incorporation into a growing B-doped diamond surface. For the purpose of this illustrative calculation, we assume that B atoms attach to radical surface sites C<sub>S</sub>\* with an incorporation probability  $\beta = 0.1$ . The rate of boron incorporation,  $R_B$ , will then be given by

$$R_B[\text{cm}^{-2}/\text{s}] = 0.1 \frac{[\text{B}]v_B}{4} \frac{C_{\text{S}}^*}{C_{\text{S}}^* + C_{\text{S}}\text{H}} \quad (17)$$

where [B] and  $v_B$  are, respectively, the concentration and the thermal velocity of B atoms just above the substrate, and  $C_{\text{S}}^*/$

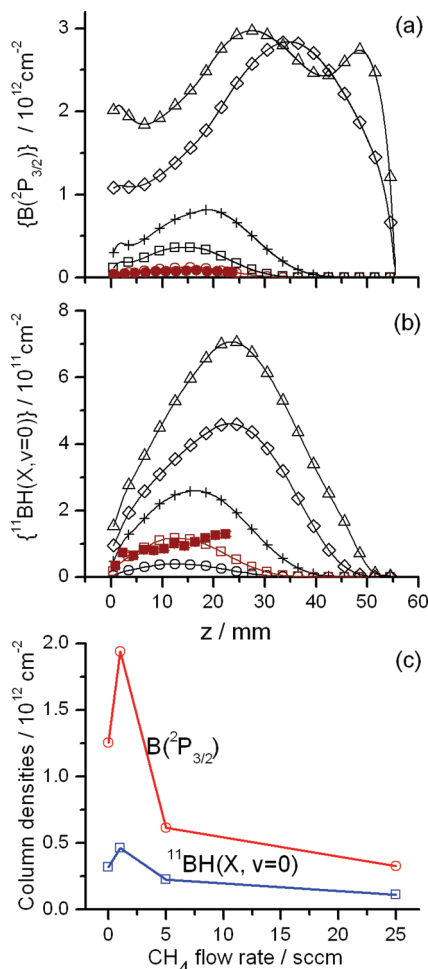


**Figure 10.** (a)  $B(^2P_{3/2})$  and (b)  $^{11}\text{BH}(X, v = 0)$  column densities predicted by the 2D model for base conditions and various  $F(\text{CH}_4)$ , plotted as functions of  $z$ :  $F(\text{B}_2\text{H}_6) = 0.003$  sccm,  $F(\text{CH}_4) = 25$  sccm, (O);  $F(\text{B}_2\text{H}_6) = 0.009$  sccm;  $F(\text{CH}_4) = 0$  sccm ( $\diamond$ ), 1 sccm ( $\Delta$ ), 5 sccm (+), 25 sccm ( $\square$ ). The solid symbols (data from Figure 5a for the appropriate  $F(\text{B}_2\text{H}_6)$ ) show the corresponding  $z$ -dependent  $\{B(^2P_{3/2})\}$  (in panel a) and  $\{^{11}\text{BH}(X, v = 0)\}$  (in panel b) values measured by CRDS under base conditions but with  $F(\text{B}_2\text{H}_6) = 0.003$  and 0.009 sccm, respectively, and the dashed vertical lines show the position of the laser beam when measuring the  $B(^2P_{3/2})$  and  $^{11}\text{BH}(X, v = 0)$  column densities as functions of the various plasma parameters in Figures 3 and 4. (c) Calculated variation in  $\{B(^2P_{3/2})\}$  and  $\{^{11}\text{BH}(X, v = 0)\}$  at  $z = 10$  mm and  $F(\text{B}_2\text{H}_6) = 0.009$  sccm plotted as a function of  $F(\text{CH}_4)$  that successfully reproduces the local maxima observed experimentally at low  $\text{CH}_4$  flow rates (Figure 4c).

$(\text{C}_5^* + \text{C}_5\text{H})$  is the fraction of radical sites on the growing diamond surface, which we take to be  $\sim 0.08$  for our base conditions.<sup>26</sup> Thus, we derive  $R_B \sim 286 \times [\text{B}] = 1.16 \times 10^{13} \text{ cm}^{-2} \text{ s}^{-1}$  at the substrate center. From our previous diamond growth modeling and calculated diamond growth rate  $G \sim 3.8 \mu\text{m/h}$ <sup>26,53</sup> we can derive the corresponding rate of carbon incorporation:  $R_C \sim 171 \times [\text{CH}_3] = 1.8 \times 10^{16} \text{ cm}^{-2} \text{ s}^{-1}$ . Thus, we arrive at an estimate of the ratio of boron and carbon incorporation rates,  $R_B/R_C \sim 6 \times 10^{-4}$ , which is comparable to the B/C ratio in the input source gases ( $2 \times F(\text{B}_2\text{H}_6)/F(\text{CH}_4) \sim 7 \times 10^{-4}$ ). Further, we note that changing the assumed probability of a B atom reacting at a  $\text{C}_5^*$  site has relatively little effect on the derived rate  $R_B$ , since any increase (decrease) of  $\beta$  results in a rather similar decrease (increase) of  $[\text{B}]$  above the substrate.

## 5. Conclusions

The potential applicability of B-doped CVD diamond is becoming ever more widely recognized. This paper reports the first comprehensive study of MW activated  $\text{B}_2\text{H}_6/\text{CH}_4/\text{Ar}/\text{H}_2$  plasmas operating under conditions relevant to commercial growth of B-doped diamond. Absolute column densities of ground state B atoms, electronically excited  $\text{H}(n = 2)$  atoms, and  $\text{BH}$ ,  $\text{CH}$ , and  $\text{C}_2$  radicals have been determined by cavity ring down spectroscopy, as functions of height ( $z$ ) above a molybdenum substrate and of the plasma process conditions (i.e., the flow rates  $F(\text{B}_2\text{H}_6)$ ,  $F(\text{CH}_4)$ ,  $F(\text{Ar})$ , pressure  $p$  and input power  $P$ ). Optical emission spectroscopy has also been used to explore variations in the relative densities of electronically excited H atoms,  $\text{H}_2$  molecules, and  $\text{BH}$ ,  $\text{CH}$ , and  $\text{C}_2$  radicals, as functions of the same process conditions. These experimental data are complemented by 2D( $r, z$ ) modeling that makes due allowance for variations in the plasma parameters and conditions (e.g., the power density  $Q$ ,  $T_e$ ,  $T_{\text{gas}}$ ,  $n_e$ , and the plasma chemistry) as functions of the same process conditions.

Comparisons between experimental and model outputs for the present  $\text{B}_2\text{H}_6/\text{CH}_4/\text{Ar}/\text{H}_2$  plasmas, and for  $\text{B}_2\text{H}_6/\text{Ar}/\text{H}_2$ <sup>32</sup> and  $\text{CH}_4/\text{Ar}/\text{H}_2$ <sup>26,29,30</sup> plasmas operating in the same MW reactor, show that trace  $\text{B}_2\text{H}_6$  additions have negligible effect on a pre-established  $\text{CH}_4/\text{Ar}/\text{H}_2$  plasma. The B and BH concentration profiles measured in a  $\text{B}_2\text{H}_6/\text{CH}_4/\text{Ar}/\text{H}_2$  plasma are less extensive than in a hydrocarbon-free  $\text{B}_2\text{H}_6/\text{Ar}/\text{H}_2$  plasma operating at the same  $p$ ,  $P$ , etc., however. Both experimental observation and the 2D modeling indicate that deposition of B-containing material on the reactor walls (mainly from B atom adsorption, with some participation from  $\text{H}_2\text{O}$ ) becomes progressively less important as  $F(\text{CH}_4)$  increases.  $\text{H}/\text{B}/\text{C}/\text{O}$  coupling reactions are deduced to play important (but still incompletely understood) roles in determining the local  $\text{BH}_x$  ( $x = 0-3$ ) number densities. Most (75–80%) of the  $\text{B}_2\text{H}_6$  in the input gas mixture is dissociated in the hot plasma (and near plasma) regions. The resulting  $\text{BH}_x$  species undergo further processing, and much of the boron is deduced to be stored as more stable  $\text{H}_x\text{B}_y\text{C}_z\text{O}_z$  reservoir species like  $\text{HBO}$ ,  $\text{H}_2\text{BO}$ ,  $\text{H}_3\text{COBH}_2$  and, particularly,  $\text{CH}_2\text{CHBH}_2$  and  $\text{CH}_3\text{CH}_2\text{BH}_2$ . The spatial profiles of the various  $\text{BH}_x$  profiles reflect the complex balance of diffusional transfers and interconversions between the various families of B containing species in the different local environments ( $T_{\text{gas}}$ ,  $[\text{H}]$ ,  $[\text{H}_2]$ ,  $[\text{H}_2\text{O}]$ ,  $[\text{C}_x\text{H}_y]$ , etc.). Key conversions in the mechanism proposed here include  $\text{BH}_x \leftrightarrow \text{H}_y\text{BC}_z$  (involving  $\text{C}_2\text{H}_2$  and  $\text{C}_2\text{H}_4$ ) and  $\text{BH}_x \rightarrow \text{H}_y\text{BO} \rightarrow \text{H}_z\text{COBH}_y \rightarrow \text{BH}_x$  (via reaction with, or activation by,  $\text{H}_2\text{O}$ ,  $\text{CH}_x$  species and/or H atoms). 2D model calculations using the proposed  $\text{H}/\text{B}/\text{C}/\text{O}$  mechanism succeed in reproducing the local “explosion” of B and BH concentrations observed when adding  $F(\text{CH}_4) \sim 1-2$  sccm to a pre-existing  $\text{B}_2\text{H}_6/\text{Ar}/\text{H}_2$  plasma. The present analysis suggests that B atom concentrations in the hot plasma region are typically  $\sim 10^{10}-10^{11} \text{ cm}^{-3}$ , and that B atoms are the most abundant gas phase  $\text{BH}_x$  species adjacent to the growing diamond surface. The estimated rate of incorporating B atoms into the growing film implies a boron doping level comparable to the B/C ratio in the input gas mixture (i.e.,  $2 \times F(\text{B}_2\text{H}_6)/F(\text{CH}_4)$ ). Future gas-surface modeling studies will investigate the energetics of elementary reaction sequences whereby such species can add to radical sites, and/or insert into C–H bonds, on a growing diamond surface.

**Acknowledgment.** M. N. R. A. is grateful to EPSRC for the award of a portfolio grant (LASER) and postdoctoral support for J. M., to Element Six Ltd. for financial support and the long term loan of the MW reactor, and to colleagues Prof. J. N.

Harvey, K. N. Rosser, and Dr. J. A. Smith for their many contributions to the work described here. Y. A. M. acknowledges support from RF Government for Key Science Schools grant No. 3322.2010.2. The Bristol-Moscow collaboration is supported by a Royal Society Joint Project Grant.

## References and Notes

- (1) Eremets, M. I. *Semicond. Sci. Technol.* **1991**, *6*, 439.
- (2) Kalish, R. *Carbon* **1999**, *37*, 781.
- (3) May, P. W. *Phil. Trans. Roy. Soc. London A* **2000**, *358*, 473.
- (4) Gicquel, A.; Hassouni, K.; Silva, F.; Achard, J. *Curr. Appl. Phys.* **2001**, *1*, 479.
- (5) Deneuville, A. *Semiconduct. Semimet.* **2003**, *76*, 183, and references therein.
- (6) Aleksov, A.; Kubovic, M.; Kaeb, N.; Spitzberg, U.; Bergmaier, A.; Dollinger, G.; Bauer, T.; Schreck, M.; Stritzker, B.; Kohn, E. *Diam. Rel. Mater.* **2003**, *12*, 391.
- (7) El-Haji, H.; Denisenko, A.; Kaiser, A.; Balmer, R. S.; Kohn, E. *Diam. Rel. Mater.* **2008**, *17*, 1259.
- (8) Willems, B. L.; Dao, V. H.; Vanacken, J.; Chibotaru, L. F.; Moshchalkov, V. V.; Guillaumon, I.; Suderow, H.; Vieira, S.; Janssens, S. D.; Williams, O. A.; Haenen, K.; Wagner, P. *Phys. Rev. B* **2009**, *80*, 224518, and references therein.
- (9) Butler, J. E.; Geis, M. W.; Krohn, K. E.; Lawless, J.; Deneault, S.; Lyszczarz, T. M.; Flechtner, D.; Wright, R. *Semicond. Sci. Technol.* **2003**, *18*, S67.
- (10) Twitchen, D. J.; Whitehead, A. J.; Coe, S. E.; Isberg, J.; Hammersberg, J.; Wikstrom, T.; Johansson, E. *IEEE Trans. Electron Devices* **2004**, *51*, 826.
- (11) Imura, M.; Liao, M. Y.; Alvarez, J.; Koide, Y. *Diam. Rel. Mater.* **2009**, *18*, 296.
- (12) Takano, Y.; Nagao, M.; Sakaguchi, I.; Tachiki, M.; Hatano, T.; Kobayashi, K.; Umezawa, H.; Kawarada, H. *Appl. Phys. Lett.* **2004**, *85*, 2851.
- (13) Ekimov, E. A.; Sidorov, V. A.; Bauer, E. D.; Mel'nik, N. N.; Curro, N. J.; Thompson, J. D.; Stishov, S. M. *Nature* **2004**, *428*, 542.
- (14) Sidorov, V. A.; Ekimov, E. A.; Stishov, S. M.; Bauer, E. D.; Thompson, J. D. *Phys. Rev. B* **2005**, *71*, 060502.
- (15) Nebel, C. E.; Rezek, B.; Shin, D.; Uetsuka, H.; Yang, N. *J. Phys. D: Appl. Phys.* **2007**, *40*, 6443.
- (16) Nebel, C. E.; Shin, D. C.; Rezek, B.; Tokuda, N.; Uetsuka, H.; Watanabe, H. *J. Roy. Soc. Interface* **2007**, *4*, 439.
- (17) Cheesman, A.; Harvey, J. N.; Ashfold, M. N. R. *Phys. Chem. Chem. Phys.* **2005**, *7*, 1121.
- (18) Gheeraert, E.; Deneuville, A.; Mambou, J. *Carbon* **1999**, *37*, 107.
- (19) Lee, B. J.; Ahn, B. T.; Baik, Y. J. *Diam. Rel. Mater.* **1999**, *8*, 251.
- (20) Ramamurti, R.; Becker, M.; Schuelke, T.; Grotjohn, T.; Reinhard, D.; Asmussen, J. *Diam. Rel. Mater.* **2008**, *17*, 1320.
- (21) Osiac, M.; Lavrov, B. P.; Röpkcke, J. *J. Quant. Spec. Radiat. Transfer* **2002**, *74*, 471.
- (22) Lavrov, B. P.; Osiac, M.; Pipa, A. V.; Röpkcke, J. *Plasma Sources Sci. Technol.* **2003**, *12*, 576.
- (23) Rayar, M.; Veis, P.; Foissac, C.; Supiot, P.; Gicquel, A. *J. Phys. D: Appl. Phys.* **2006**, *39*, 2151.
- (24) Comerford, D. W.; Cheesman, A.; Carpenter, T. P. F.; Davies, D. M. E.; Fox, N. A.; Sage, R. S.; Smith, J. A.; Ashfold, M. N. R.; Mankelevich, Y. A. *J. Phys. Chem. A* **2006**, *110*, 2868.
- (25) Rayar, M.; Supiot, P.; Veis, P.; Gicquel, A. *J. Appl. Phys.* **2008**, *104*, 033304.
- (26) Mankelevich, Y. A.; Ashfold, M. N. R.; Ma, J. *J. Appl. Phys.* **2008**, *104*, 113304.
- (27) Cheesman, A.; Smith, J. A.; Ashfold, M. N. R.; Langford, N.; Wright, S.; Duxbury, G. *J. Phys. Chem. A* **2006**, *110*, 2821.
- (28) Ma, J.; Cheesman, A.; Ashfold, M. N. R.; Hay, K. G.; Wright, S.; Langford, N.; Duxbury, G.; Mankelevich, Y. A. *J. Appl. Phys.* **2009**, *106*, 033305.
- (29) Ma, J.; Richley, J. C.; Ashfold, M. N. R.; Mankelevich, Y. A. *J. Appl. Phys.* **2008**, *104*, 103305.
- (30) Ma, J.; Ashfold, M. N. R.; Mankelevich, Y. A. *J. Appl. Phys.* **2009**, *105*, 043302.
- (31) Butler, J. E.; Mankelevich, Y. A.; Cheesman, A.; Ma, J.; Ashfold, M. N. R. *J. Phys. Condens. Matter* **2009**, *21*, 364201.
- (32) Ma, J.; Richley, J. C.; Davies, D. R. W.; Cheesman, A.; Ashfold, M. N. R.; Mankelevich, Y. A. *J. Phys. Chem. A* **2010**, *114*, 2447.
- (33) Western, C. M.; *PGOPHER, a Program for Simulating Rotational Structure*; University of Bristol: <http://pgopher.chm.bris.ac.uk>.
- (34) Fox, O. J. L.; Ma, J.; May, P. W.; Ashfold, M. N. R.; Mankelevich, Y. A. *Diam. Rel. Mater.* **2009**, *18*, 750.
- (35) Mankelevich, Y. A.; May, P. W. *Diam. Rel. Mater.* **2008**, *17*, 1021.
- (36) Smith, G. P.; Golden, D. M.; Frenklach, M.; Moriarty, N. W.; Eiteneer, B.; Goldenberg, C. T.; Bowman, C. T.; Hanson, R. K.; Song, C.; Gardiner, Jr., W. C.; Lissianski, V. V.; Qin, Z.; <http://www.me.berkeley.edu/gri-mech>.
- (37) Hassouni, K.; Gicquel, A.; Capitelli, M.; Loureiro, J. *Plasma Sources Sci. Technol.* **1999**, *8*, 494.
- (38) Nagase, S.; Ray, N. K.; Morokuma, K. *J. Am. Chem. Soc.* **1980**, *102*, 4536.
- (39) Wang, X.; Li, Y.; Wu, Y.-D.; Paddon-Row, M. N.; Rondan, N. G.; Houk, K. N. *J. Org. Chem.* **1990**, *55*, 2601.
- (40) Garland, N. L.; Stanton, C. T.; Fleming, J. W.; Baronavski, A. P.; Nelson, H. H. *J. Phys. Chem.* **1990**, *94*, 4952.
- (41) McKee, N. L. *J. Am. Chem. Soc.* **1995**, *117*, 8001.
- (42) Pasternack, L.; Balla, R. J.; Nelson, H. H. *J. Phys. Chem.* **1988**, *92*, 1200.
- (43) Fehlner, T. P. *Int. J. Chem. Kin.* **1975**, *7*, 633.
- (44) Yetter, R. A.; Rabitz, H.; Dryer, F. L.; Brown, R. C.; Kolb, C. E. *Combust. Flame* **1991**, *83*, 43.
- (45) Pasternack, L. *Combust. Flame* **1992**, *90*, 259.
- (46) Garland, N. L.; Stanton, C. T.; Nelson, H. H.; Page, M. *J. Chem. Phys.* **1991**, *95*, 2511.
- (47) Chin, C.-H.; Mebel, A. M.; Hwang, D. Y. *J. Phys. Chem. A* **2004**, *108*, 473.
- (48) Weiss, N. G. *J. Am. Chem. Soc.* **1953**, *75*, 1221.
- (49) Kawashima, Y.; Takeo, H.; Matsumura, C. *J. Chem. Phys.* **1981**, *74*, 5430.
- (50) Linstrom, P. J.; Mallard, W. G., Eds. *NIST Chemistry WebBook, NIST Standard Reference Database Number 69*; National Institute of Standards and Technology: Gaithersburg MD, 20899; <http://webbook.nist.gov>, (retrieved April 7, 2010).
- (51) Frisch, M. J.; Trucks, G. W.; Schlegel, H. B.; Scuseria, G. E.; Robb, M. A.; Cheeseman, J. R.; Montgomery, Jr., J. A.; Vreven, T.; Kudin, K. N.; Burant, J. C.; Millam, J. M.; Iyengar, S. S.; Tomasi, J.; Barone, V.; Mennucci, B.; Cossi, M.; Scalmani, G.; Rega, N.; Petersson, G. A.; Nakatsuji, H.; Hada, M.; Ehara, M.; Toyota, K.; Fukuda, R.; Hasegawa, J.; Ishida, M.; Nakajima, T.; Honda, Y.; Kitao, O.; Nakai, H.; Klene, M.; Li, X.; Knox, J. E.; Hratchian, H. P.; Cross, J. B.; Adamo, C.; Jaramillo, J.; Gomperts, R.; Stratmann, R. E.; Yazyev, O.; Austin, A. J.; Cammi, R.; Pomelli, C.; Ochterski, J. W.; Ayala, P. Y.; Morokuma, K.; Voth, G. A.; Salvador, P.; Dannenberg, J. J.; Zakrzewski, V. G.; Dapprich, S.; Daniels, A. D.; Strain, M. C.; Farkas, O.; Malick, D. K.; Rabuck, A. D.; Raghavachari, K.; Foresman, J. B.; Ortiz, J. V.; Cui, Q.; Baboul, A. G.; Clifford, S.; Cioslowski, J.; Stefanov, B. B.; Liu, G.; Liashenko, A.; Piskorz, P.; Komaromi, I.; Martin, R. L.; Fox, D. J.; Keith, T.; Al-Laham, M. A.; Peng, C. Y.; Nanayakkara, A.; Challacombe, M.; Gill, P. M. W.; Johnson, B.; Chen, W.; Wong, M. W.; Gonzalez, C.; Pople, J. A. *Gaussian 03, Revision B.04*; Gaussian, Inc.: Pittsburgh PA, 2003.
- (52) Kawashima, Y.; Takeo, H.; Matsumura, C. *J. Mol. Spectrosc.* **1986**, *116*, 23.
- (53) May, P. W.; Mankelevich, Y. A. *J. Phys. Chem. C* **2008**, *112*, 12432.